

RAM

● ROBOTICS
AND
MECHATRONICS

CATHETER MODELLING AND FORCE ESTIMATION IN ENDOVASCULAR APPLICATIONS

C. (Chenhao) Li

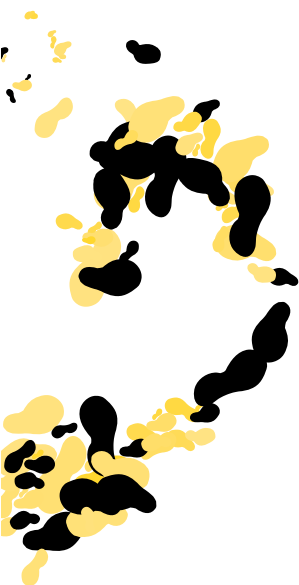
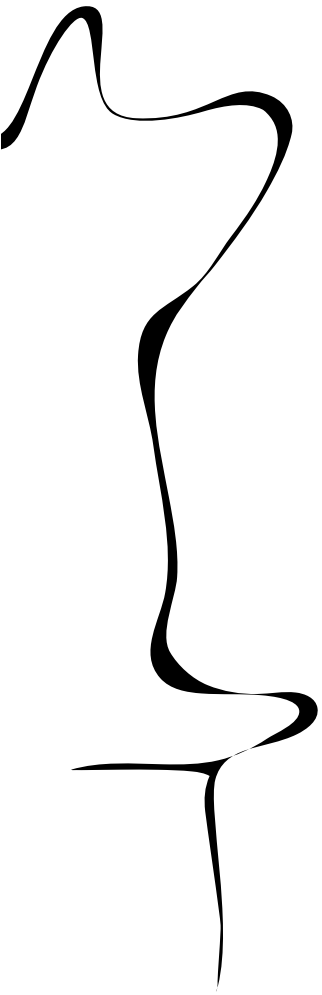
MSC ASSIGNMENT

Committee:

prof. dr. ir. S. Stramigioli
dr. G. Dagnino
Dr.-Ing. D. Kundrat
dr. ir. B.J.F. van Beijnum

January, 2023

001RaM2023
Robotics and Mechatronics
EEMathCS
University of Twente
P.O. Box 217
7500 AE Enschede
The Netherlands



Abstract

Cardiovascular disease (CVD) is the leading cause of death worldwide. As a minimally invasive treatment, vascular interventional therapy has been widely used in different disciplines such as vascular surgery, cardiovascular surgery, and neurosurgery. Robotic platforms have been designed to assist surgeons, in order to increase accuracy, repeatability, comfort, and post-operative recovery times. One major limitation of endovascular robotic platforms with respect to the manual approach is the lack of direct contact with the fingers and instruments. The loss of tactile sense will make the operator's hand-eye coordination difficult. Especially in the process of vascular intervention, it is difficult for doctors to estimate the operation force only by imaging e.g., fluoroscopy, which may easily cause blood vessel rupture.

In this thesis, inspired by robotic platform for endovascular interventions – CathBot (developed at the Imperial College London), a physical model-based method is proposed to estimate the contact force of the catheter. A catheter model is established based on beam theory, and a 3D vascular model of the abdominal aorta (silicon phantom) is reconstructed from CT data. The contact between the catheter and the phantom model is detected and friction is considered for the simulation of the catheterization process using a simulation framework (SOFA). Experiments are set up to measure the contact force as well as the catheter position during actual insertion process. The proposed method estimates the contact force on the whole catheter during the insertion process with an average error of 0.04N with respect to the experiment results. The position of the catheter tip obtained by simulation is within the acceptable error range (average error 3.1mm respect to the experiment results), and the configuration of the whole catheter can be obtained.

Content

Abstract.....	i
Content.....	ii
1. Introduction.....	1
1.1 Background.....	1
1.1.1 Endovascular interventions.....	1
1.1.2 Cathbot.....	2
1.2 Related work.....	4
1.3 Objectives of this research.....	5
2. Resources and Methods.....	5
2.1 Resources.....	6
2.1.1 SOFA framework.....	6
2.1.2 Phantom model.....	8
2.1.3 Catheters.....	8
2.2 Mechanical Deformation Model of Catheter.....	9
2.2.1 Physics-based model based on beam theory.....	9
2.1.2 Co-rotational finite element approach.....	10
2.2.2 Dynamics of deformable model and implicit integration.....	12
2.3 Mechanical Deformation Model of Phantom.....	12
2.3.1 from CT&MRI to surface mesh.....	12
2.3.2 Rigid surface model and volume deformation model of phantom in SOFA frame work.....	15
2.4 Constraint.....	17
2.4.1 Fixed constraint of phantom.....	17
2.4.2 Contact constraint.....	18
2.4.3 Constraint-based solution (Lagrange multipliers).....	21
3. Experiment and Result.....	22
3.1 Simulation setting.....	22
3.2 Catheter insertion &force measurement.....	24
3.3 Configuration extraction.....	26
3.4 Results and discussion.....	29
3.4.1 Results.....	29
3.4.2 Discussion.....	37
4. Conclusions and Future Directions.....	39
4.1 Conclusions.....	39
4.2 Open Challenges and Future Directions.....	39
Bibliography.....	41

1. Introduction

1.1 Background

1.1.1 Endovascular interventions

Cardiovascular disease (CVD) is the leading cause of death worldwide, claiming an estimated 17.9 million lives annually [1]. Cardiovascular disease is a group of heart and blood vessel diseases, including coronary heart disease, cerebrovascular disease, rheumatic heart disease and other diseases. As a minimally invasive treatment, vascular interventional therapy has been widely used in different disciplines such as vascular surgery, cardiovascular surgery, and neurosurgery. Traditional vascular interventional surgery relies on fluoroscopy to operate the catheter guide wire, which has certain problems in sustainability and accuracy. Endovascular surgery is performed by manipulating guidewires and catheters through the vasculature in order to reach areas of interest where treatment is needed (e.g., stenting, ablation, embolization, device delivery). These procedures require only a small incision, through which long and thin instruments are inserted. Using image guidance (X-Ray angiography, Magnetic Resonance Angiogram), the catheter is guided through a blood vessel to perform the required treatment [2]. At the same time, the operator bears a high risk of occupational hazards [3] in the long-term X-ray exposure and the weight of the lead protective apron.

Endovascular robotic technology may help overcome many of the challenges associated with traditional endovascular techniques. Several robotic systems have been developed to perform a broad range of endovascular procedures. In 2015 Magellan robotic system approved for peripheral vascular interventions [4]. Magellan robotic system consists of a remote electromechanical operator workstation and a robotic arm that delivers a steerable catheter [5]. This system allows control of the robotic arm from a remote workstation to steer catheter movement. The Amigo remote catheter system [6] (Catheter Precision Inc) is an electromechanical system that uses remote manipulation of a standard steerable electrophysiology catheter. Another robotic platform Cathbot will be specifically mentioned in Section 1.12.

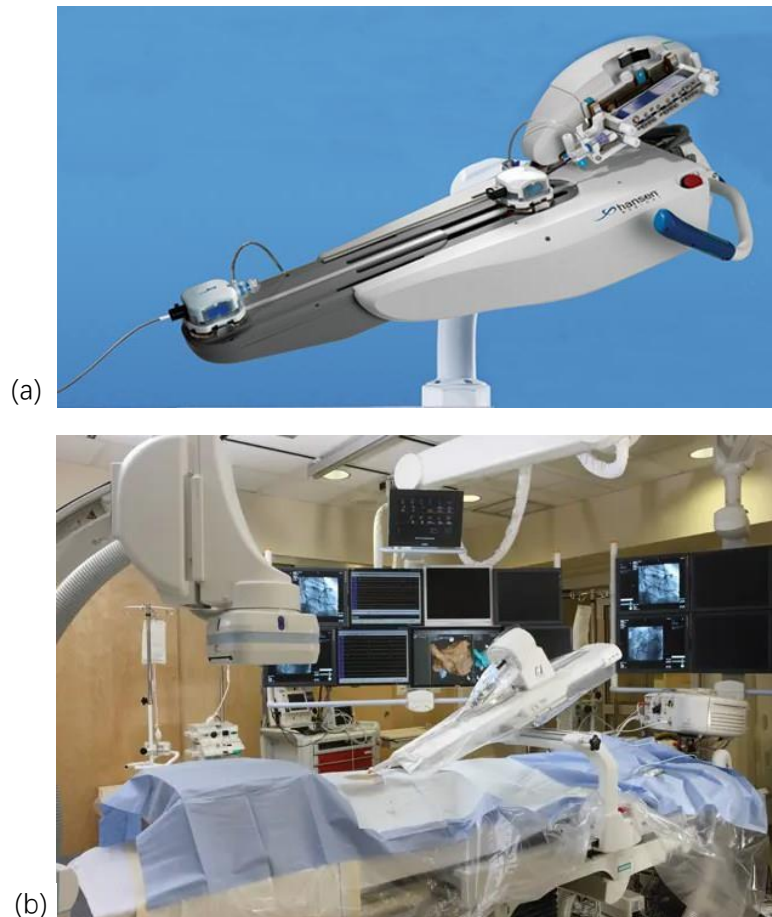


Figure 1.1 Example of Endovascular robotic platform: (a): Magellan [5]; (b): Amigo [6].

Advantages of the endovascular robotics include improved dexterity and precision, reduced vessel wall contact, less radiation exposure for the operator, and an ergonomic working position for the clinician. A disadvantage of these telerobotic navigation systems is the lack of tactile or force feedback during manipulation of wires, catheters or devices.

Due to difficult hand-eye coordination, complicated looping and bending of the instruments and the risk of vessel injury, these techniques need to be performed by highly trained and experienced specialists. Some especially risky procedures are even expected to require specific certification and training [7]. In order to reduce the hand-eye coordination difficulties caused by the loss of tactile sense, it is necessary to combine force feedback technology in vascular interventional surgery robots.

1.1.2 Cathbot

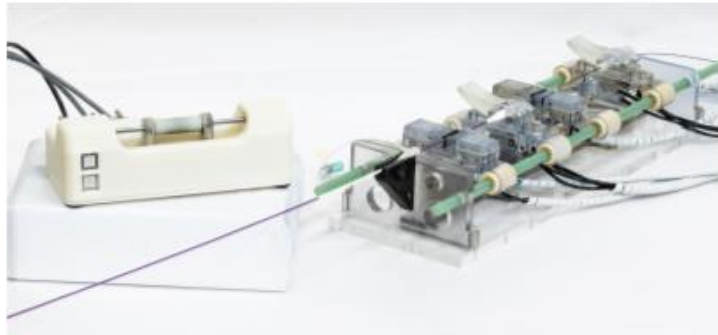
CathBot [8] is a novel teleoperated robotic platform for fluoroscopy and MRI-guided endovascular interventions. The system aims at addressing the following clinical requirements:

- a.) Compatibility with different imaging modalities, e.g., fluoroscopy or MRI;
- b.) Versatility: for performing a wide range of vascular interventions;
- c.) State of the art navigation system: for minimizing contacts between the manipulated

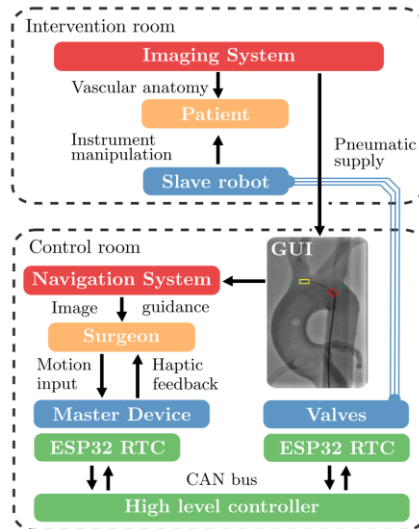
instrument and the vasculature;

- d.) Teleoperation: for increased comfort of the surgeon, also to move the surgeon out of the room and reduce the exposure to x-ray radiations.

The robot is designed as a master-slave device. The master device [9] is designed to mimic and map the established manual intra-procedural handling of standard catheters and guidewires. In this regard, the manipulator has a cylindrical handle that imitates the interaction and executable DOF (degree of freedom) (i.e., feeding / retraction and rotation) of standard catheters and guidewires. This design improves the teleoperation transparency, while keeping the controls intuitive for the user. A linear and a rotary brushless DC motors are used in order to provide haptic feedback for linear motion (feeding/retraction), and rotational motion respectively.



(a)



(b)

Fig 1.2. Cathbot platform: (a): MR-safe slave robot (right) and intuitive master device (left); (b): System architecture of Cathbot. The surgeon in the control room teleoperates the MR-safe slave robot deployed in the intervention room with the master device. The navigation system provides real-time visual guidance and haptic feedback is rendered through the master device to guide the surgeon during the procedure [10].

A dynamic active constraint (DAC) with safety margins (adaptively enforced in real-time to constrain the catheter motion) are developed and integrated into the navigation system to provide vision-based haptic feedback [9]

The platform task performance was evaluated in an ex vivo cannulation study with clinical experts under fluoroscopic guidance and haptic assistance on abdominal and thoracic phantoms. The results show using this platform enabled successful remote cannulation of different vascular anatomies with success rates of 90%–100% [10]. And its clinical usability was demonstrated through in-vivo animal trials [11].

1.2 Related work

This work is based on the content of Cathbot to make further improvements to the force feedback system. In the force feedback system of Cathbot, Dagnino, G. et al. define the direction and magnitude of the contact force by tracking the relative position of the vessel wall and catheter tip in the image, to minimize the risk of damages to the vessel and potentially improving the overall precision and safety [9]. In addition, there are many vision-based works to calculate the posture of surgical equipment in the blood vessel and the relative position information to the blood vessel wall. Recent approaches have leveraged deep learning techniques to recover the depth of a full field fluoroscopic image [12], but they fail to recover fine structures such as catheters except for very specific shapes [13]. In such cases 3D reconstruction is required. However, retrieving the 3D shape of an object from 2D features is an ill-posed problem: due to missing depth information, several 3D shapes may correspond to a given 2D configuration. For endovascular interventions, one possible solution is to use bi-plane imaging systems in order to overcome the ambiguity of 2D images [14]. However, the wide baseline and the lack of texture makes image features extraction and matching more difficult, and requires more fluoroscopy equipment, such as c-arms and redundant X-ray machines, which also increases the cost of surgery. And if we want to get the force distribution on the catheter, we need to use the inverse finite element method to calculate after the attitude is obtained [15]. The calculation is computationally expensive and the load distribution across the catheter must be assumed in advance by confirming the contact position.

Compared with the method of reconstructing the catheter model from the image, the method based on the physical model can provide better descriptions and overcome the above limitations. By physically-based modeling of the kinematics and dynamics of the interventional device (catheters) and the contact environment (vessels, tissues), it is possible to perform operations on known inputs (surgical operator actions: insertion, extraction, rotation) to simulate the motion of the interventional device to obtain the 3D shape and the applied force of the target [16]. For the physical model of the catheter, Dawson et al. [17] firstly employed a set of rigid links connected by joints to simulate catheters where the catheter was moved by three forces, such as contact force, injection force, and forces exerted by users. However, this model cannot realistically simulate the complex behaviors of catheters in catheterization. A simple spring-damper model is used to simulate the cannulation procedure of ERCP (Endoscopic Retrograde Cholangial-Pancreatography) [18], but this rough spring damping model has poor system stability and exist the delay in the propagation of force effects [18]. Cotin et al. [19] model the catheter with a set of linked deformable beams.

They proposed an incremental finite element method (FEM) built on the strain-stress model of the beams for catheter simulation. This method provides a more accurate description and simulation of flexible, long, and thin structures (catheters, guidewires). In this paper, the catheter modeling approach is based on this method. And most of the catheter-vessel contact simulations only focus on the force on the catheter tip [20] and ignore the effect of friction [19].

1.3 Objectives of this research

In this work, we use catheter finite element model based on beam theory [19] and elastic FEM-based vascular deformation model to simulate the contact between catheter and blood vessel, and consider non-interpenetrating conditions and friction to constrain the contact during catheter insertion. The purpose is to obtain the position information of the catheter during insertion and the contact force on the entire catheter.

Based on previous work on the Cathbot platform [9], in order to improve the accuracy of the description of the contact force to the real scene and reduce the dependence of the haptic feedback system on the image accuracy, a simulation method based on a physical model is used in this paper to estimate the configuration and contact force during catheterization in real time. Set the following goals for the overall work:

1. Build physical models of catheters and vasculature;
2. Consider friction and collisions to build the motion constraints model of catheter and contacts;
3. Simulate the insertion process of the model and set up experiments to evaluate the contact forces and catheter position obtained from simulation.

2. Resources and Methods

The main purpose of this work is to simulate the process of catheter insertion into blood vessels based on physical models, and obtain model-based catheter deformation and contact forces based on physical constraints. In order to achieve this, this paper divides the mission objectives into three phases:

1. Establish a physical model of the catheter based on beam theory [21], and solve the model through an efficient co-rotational finite element (FE) approach [22]; (Section 2.2)
2. Based on unstructured grid modeled the volume deformation model of the phantom using FEM approach; (Section 2.3)
3. Perform Collision detection using the *LocalMinDistance* method in SOFA and define constraints considering boundary non-interpenetration and friction laws. (Section 2.4)

2.1 Resources

In the following, I describe the software platform used for catheterization simulation in section 2.1.1, and introduce the catheter and vasculature model used in the experiment in section 2.1.2 and section 2.1.3.

2.1.1 SOFA framework

SOFA framework [23,24,25] is an efficient framework dedicated to research, prototyping and development of physics-based simulations, with an emphasis on medical simulation. Based on C++, the SOFA engine is build using a flexible architecture. In this paper, the simulation is implemented using this platform.

SOFA introduces the concept of scene graph-based multi-model representation to easily build simulations composed of an arbitrary number of objects. The pool of simulated objects and algorithms used in a simulation (also called a scene) is described using a hierarchical data structure similar to scene graphs used in graphics libraries (see figure 2.1). The simulated objects are decomposed into collections of independent components, each of them describing one feature of the model, such as state vectors, mass, forces, constraints, topology, integration scheme, and solving process. The generation of the scene file is written by xml code, and the sofapython3 plugin can also be compiled to embed a python3 interpreter into an existing SOFA application and to create/launch SOFA simulations from a python environment.

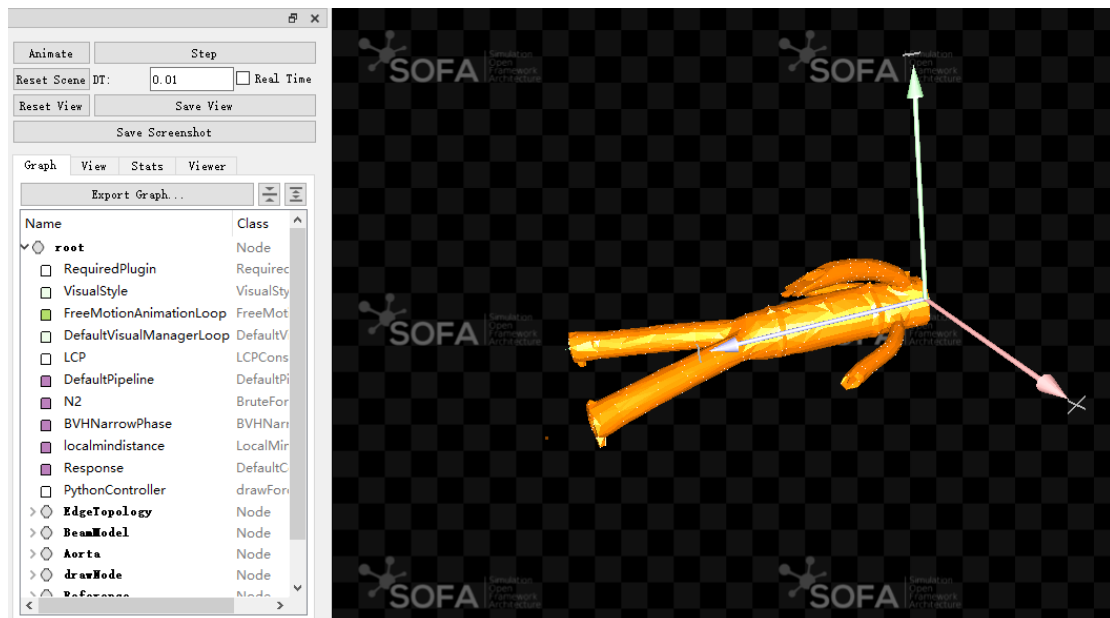
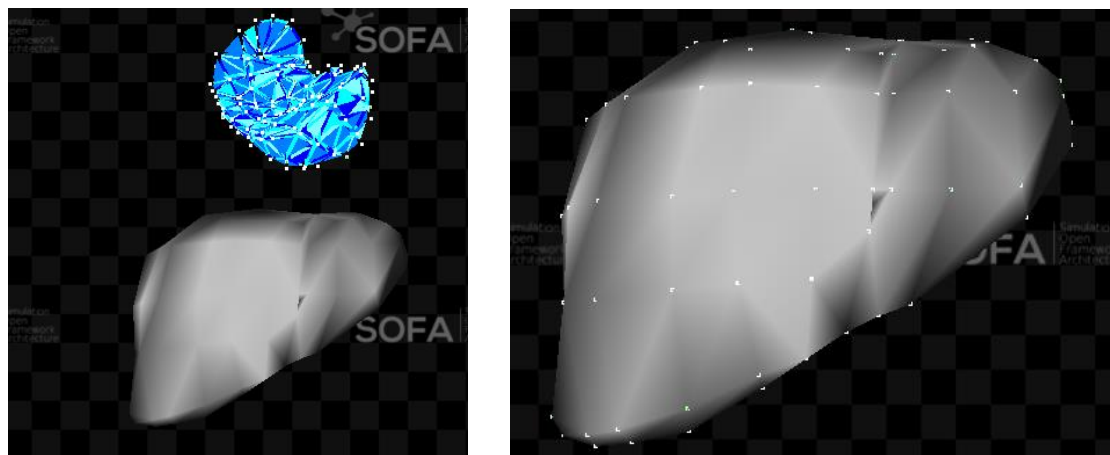


Figure 2.1 Scene graph example in SOFA: The left list shows the scene graph components and their relationships, and the right area shows the simulation animation.

In addition to highly modularity, it is possible to go one step further and decompose

simulated objects into a set of specialized models. A physical object in SOFA is typically described using three models: an internal model with the independent degrees of freedom (DOFs), the mass and the constitutive laws, a collision model with contact geometry, and a visual model with detailed geometry and rendering parameters. Each model can be designed independently of the others, and more complex combinations are possible. During run-time, the models are synchronized using a generic mechanism called mapping to propagate forces and displacements. For example, as shown in Figure 2.2, Load the volume mesh model and surface mesh model (gray) of the liver into SOFA separately, and build the elastic deformation model (blue) for the volume mesh model. Apply force to the deformed model, the surface model will move with the deformed model only when there is a topological mapping between the two models.

In our simulation, we mainly use 2 models: use the internal model to create the deformation model of the object, and use the collision model to detect the collision.



(a)

(b)

Figure 2.2 liver models in SOFA left: models without topological mapping right: models with topological mapping.

2.1.2 . Phantom model

During the experiment and simulation, the vasculature model which the catheter is inserted in is shown in Figure 2.3, referred to as 'the phantom'. The phantom is property of RAM. This abdominal model contains iliac arteries, abdominal aorta, renal arteries and superior mesenteric models. The phantom has connectors to simulate blood flow, but these were closed off since there was no pump available.

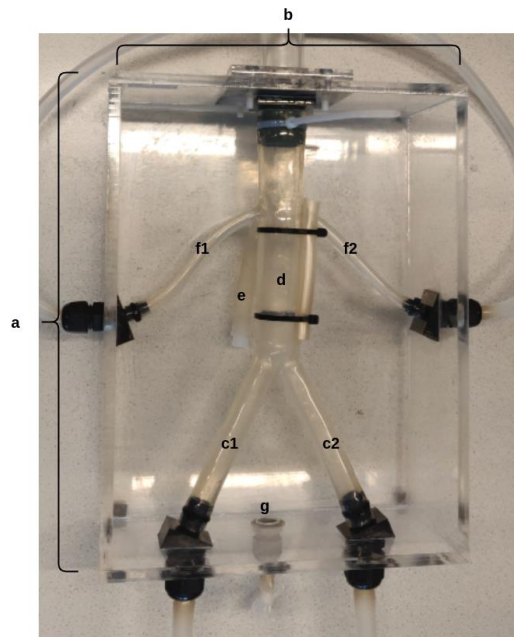


Figure2.3: The phantom used for data acquisition. The box is 30cm (a) by 23cm (b). The iliac arteries (c1, c2) are 19mm in diameter. The abdominal aorta (d) is 31 mm in diameter. The renal arteries (f1, f2) are also present, as well as the superior mesenteric (e). The surrounding box can be filled with water flow through g.

The phantom model was scanned using MRI and CT to reconstruct its 3D model to be imported in SOFA.

2.1.3 Catheters

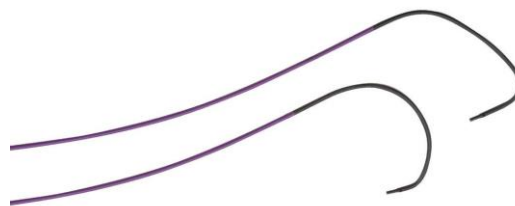


Figure2.4 Impress hydrophilic catheters with different tip form

The catheter used in the experiment were Impress hydrophilic catheters. Parameters of catheter shape can be found on the website [26] by its number. Other Specific parameters are mentioned in Section 3.1.

Catalog Nr.	Expanded family name	Length	Tip shape	Diameter
48038MHK-H	Diagnostic Peripheral	80mm	Modified Hook	1.32mm

Table 2.1. Parameters of catheter shape [26]

2.2 Mechanical Deformation Model of Catheter

2.2.1 Physics-based model based on beam theory

In the process of simulating the catheter, this work uses the *Beamadapter* plugin [27] in SOFA software. This plugin based on an incremental finite element model. Catheters are flexible but inextensible slender wire-like structures with high tensile strength and low resistance to bending. In order to describe the deformation of such linear objects, a representation has been used based on three-dimensional beam theory [28], where the elementary stiffness matrix of a single beam element is a 12×12 symmetric matrix (6 forces and 6 torques) that relates angular and spatial positions of each end of a beam element to the forces and torques applied to them: Figure2.5 shows the force diagram of the beam element.

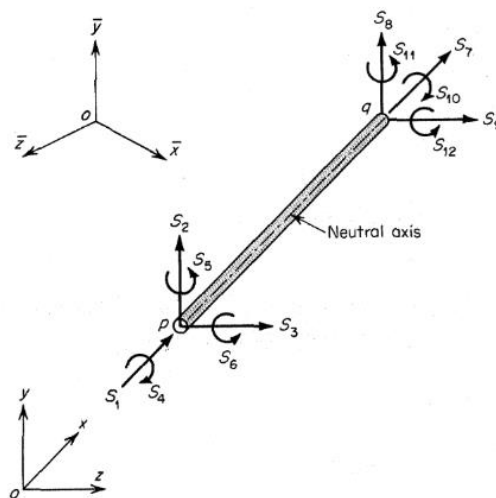


Figure2.5: Force diagram of the beam element [27].

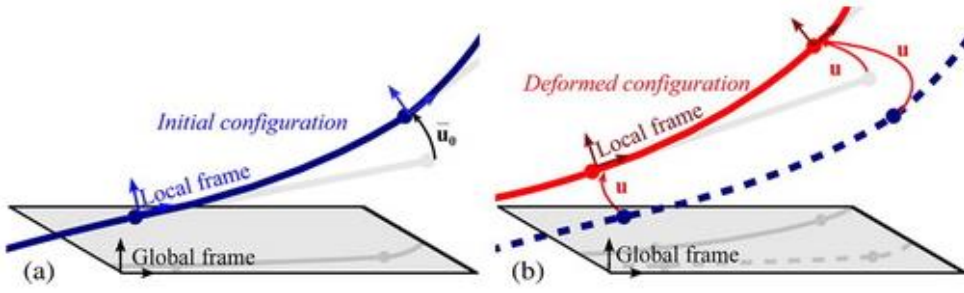


Figure 2.7 Initial (blue) and deformed (red) configurations a) initial displacement \bar{u}_0 (when the initial configuration is curved) b) deformation \bar{u} measured in the local frame [19].

In order to derive transformation matrix which can represent relationship between the element displacement \bar{u} in the local coordinate system and the element displacement u in the global coordinates, from figure 2.7 we assume displacements from initial configuration to deformed configuration are measured using u in the global reference frame and by $\bar{u} - \bar{u}_0$ in the local frame. Thus, the relationship is expressed by the matrix equation:

$$\bar{u} - \bar{u}_0 = Au \quad (2.1)$$

Where A is a matrix of coefficients obtained from the direction cosines of angles between the local and global coordinate systems and \bar{u}_0 reflects the initial configuration of the beam.

As the resulting virtual work must be independent of the coordinate system [20], it follows that:

$$\delta \bar{u}^T \bar{f} - \delta u^T f = 0 \Leftrightarrow \delta u^T (A^T \bar{f} - f) = 0 \Leftrightarrow A^T \bar{f} - f = 0 \quad (2.2)$$

Consider (2.1) and (2.2), we obtain:

$$f = [A \bar{K}_e A] u \quad (2.3)$$

Which represent the relationship of force and displacement in global coordinates.

For the entire catheter model, as we serially link a series of beam elements (see figure 2.8), the global stiffness matrix K is computed by summing the contributions of each element, thus equilibrium equation is obtained:

$$Ku = f \quad (2.4)$$

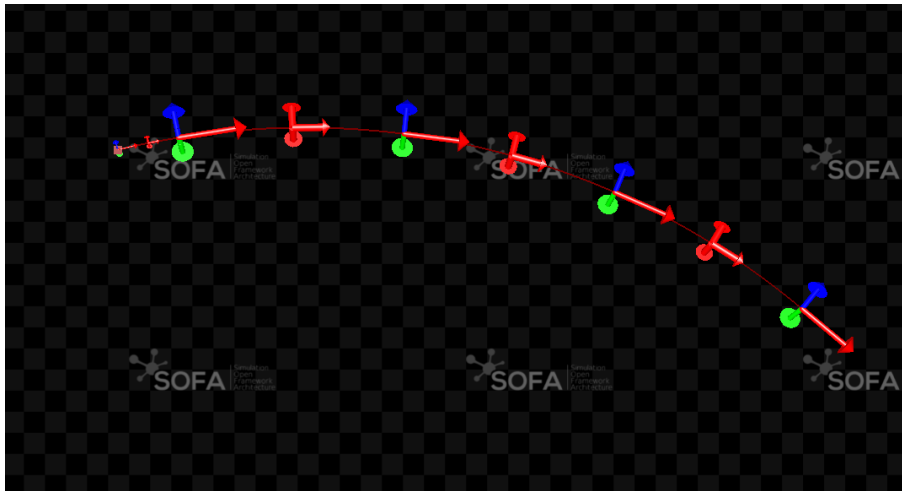


Figure 2.8: Serially link a series of beam elements to model the catheter.

2.2.2 Dynamics of deformable model and implicit integration

The dynamics of the catheter model can be described by Newton's second law of motion:

$$\mathbf{M}(\mathbf{x})\ddot{\mathbf{x}} = \mathbf{F}(t) - \mathbf{f}(\mathbf{x}, \dot{\mathbf{x}}) + \mathbf{W}(\mathbf{x}, \dot{\mathbf{x}}) \quad (2.5)$$

Where $\mathbf{x}, \dot{\mathbf{x}}, \ddot{\mathbf{x}}$ express the state (position, velocity, acceleration) of catheter model's nodes, $\mathbf{M}(\mathbf{x})$ and $\mathbf{f}(\mathbf{x}, \dot{\mathbf{x}})$ represent respectively the inertia matrix and the internal forces, both derived from the co-rotational FE model and $\mathbf{F}(t)$ expresses the external forces, while $\mathbf{W}(\mathbf{x}, \dot{\mathbf{x}})$ formalizes the boundary conditions applied to the model, which will be detailed in section 2.4 collision constraint.

All dynamic simulations assume to discretize the temporal evolution of the system through small time steps. This time step is usually noted dt . An integration scheme is the numerical method describing how to find the approximate solution for ordinary differential equations. In this case, a time-stepping method based on implicit integration method (Backward Euler method).

An implicit scheme means that the new time step ($t + dt$) is computed based on information of this next time step ($t + dt$):

$$\mathbf{y}(t + dt) = \mathbf{y}(t) + dt * \mathbf{f}(\mathbf{y}(t + dt)) \quad (2.6)$$

Thus, the discrete variables of states are expressed as:

$$\Delta \mathbf{x} = \mathbf{x}(t + T) - \mathbf{x}(t) \quad (2.7)$$

$$\Delta \mathbf{v} = \mathbf{v}(t + T) - \mathbf{v}(t) \quad (2.8)$$

Where T is the time-step.

After linearization for Non-linear terms (first-order Taylor expansion), combined with eq. (2.5), the implicit velocity update is then computed as:

$$\left(\mathbf{M} - T \frac{\partial \mathbf{f}}{\partial \mathbf{v}} - T^2 \frac{\partial \mathbf{f}}{\partial \mathbf{x}} \right) \Delta \mathbf{v} = T \left(\mathbf{f} + T \frac{\partial \mathbf{f}}{\partial \mathbf{x}} \mathbf{v} \right) + T \mathbf{J}^T \boldsymbol{\lambda} \quad (2.9)$$

Where the term $\mathbf{J}^T \boldsymbol{\lambda}$ expresses the linearized contacts, which will be detailed in section 2.3

2.3 Mechanical Deformation Model of Phantom

In this part, the DICOM data of phantom obtained from CT and MRI is compared, and the surface mesh model of phantom is extracted from the CT scan data, the volume mesh model is generated using the surface mesh model. Then the elastic deformation model was created based on the mesh model and the *TetrahedronFEMForceField* element in SOFA

2.3.1 from CT&MRI to surface mesh

We have 2 kinds of source to build phantom model, MRI & CT. import MRI data to the 3dslicer, using threshold-based segmentation, we get a rough mesh result of phantom model. with 1,127,556 vertices and 2,295,300 faces.

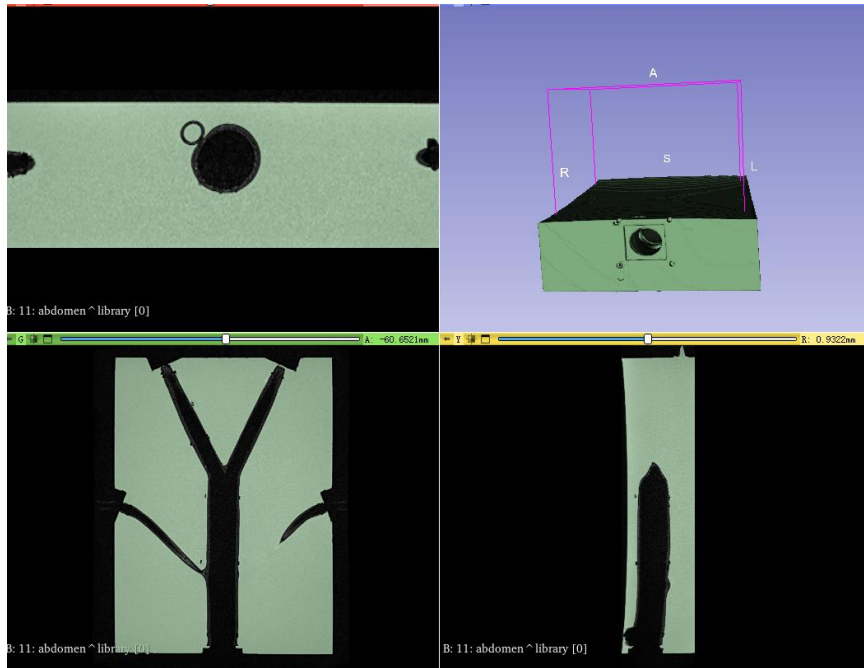


Figure 2.9 Using threshold to segment the Phantom in 3dslicer.

Then we imported this mesh to MeshLab to optimize the mesh. From the original mesh (figure 2.9 left), we can find that lots of noise exists and the number of vertices and faces are too large which will affect solution speed.

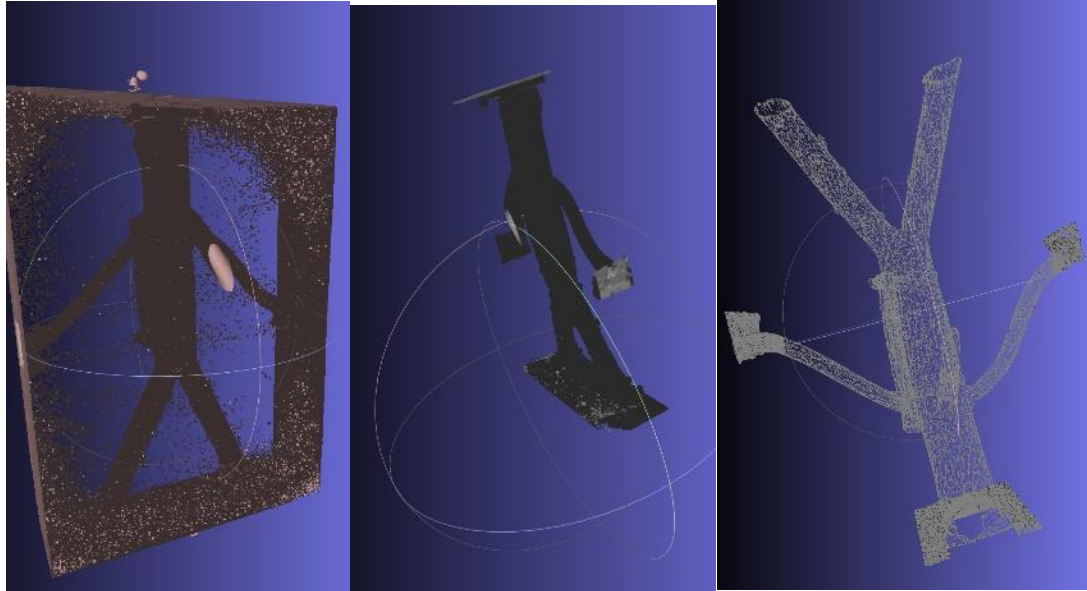


Figure 2.10 MRI mesh processing.

Thus in meshlab, the original mesh is processed as follows:

1. Select and crop a region of interest. As we can see from figure 2.3, during catheter insertion, the only part that interacts with the catheter is the elastic part (contains c1,c2,d,e,f1,f2), so the outer box was delete;
2. Then small isolated connected components were deleted by setting threshold(max

- diameter of isolated pieces) and the unreferenced vertices were removed.
3. After these cleaning process, using QEM[30] to simplify the mesh, which is a continuous and local method, and its essence is to greedily find point pairs locally for contraction. The QEM algorithm is based on a basic local operation: edge shrinkage. Shrinking an edge on the surface of a manifold triangular mesh will reduce the number of vertices by one and the number of triangles by one or two, as shown in the figure below.

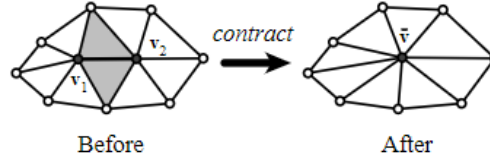


Figure 2.11 QEM method [29].

This algorithm is integrated in MeshLab as a filter function [31] and can choose whether to preserve the boundary of the mesh. After cleaning and simplification, the mesh was smoothed using the Laplacian method [31] to deal with surface noise. The principle of the simple Laplacian smoothing algorithm is to move each vertex to the average position of adjacent vertices, that is, to use the so-called umbrella operator:

$$U(p) = \frac{1}{n} \sum_{i=u}^{n-1} Adj_i(p) \quad (2.10)$$

Such a process is represented in the umbrella structure as follows:

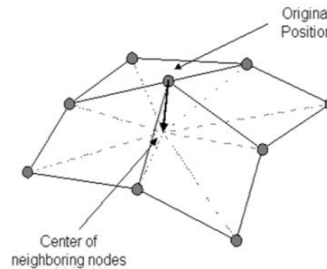


Figure 2.12 Umbrella structure in Laplacian method [32].

Its implementation logic is expressed as follows:

- a). Initialize the Mesh's adjacency point structure set
- b). Create a new temporary point set to store the smoothed position of the point
- c). For each vertices P in Mesh do:
 - Initialize temporary vector to zero vector
 - Get the neighborhood point set $Adj(P)$ of P
 - For all domain points T, add their positions to the temporary vector
 - temporary vector/= number of field point sets
 - store the position of the temporary vector into the temporary point set
- d). For all vertices P in Mesh do:
 - Modify the position of P to the position of the corresponding point in the temporary point set

Finally, the surface mesh of the phantom is obtained, which contains 40,219(96.4% reduction) vertices and 78,548(96.6%reduction) triangular faces (in figure 2.10 right).

However, since MRI is not sensitive to the material of the vessel wall model and the result have lots of noise, we end up with only a surface mesh of the inner vessel wall. In order to obtain a more accurate surface model of the phantom, we use the data obtained from CT scans. Since the data format is IMA (Siemens special format), first use NIFTI Converter to convert the scan results into loadable NIFTI image files, and import them into 3dslicer. Comparing the CT results and MRI results (see from figure2.13), segmentation will be clearer and more accurate based on the CT results. Finally, using the processing method similar to the above, the complete phantom surface mesh is obtained (figure 2.14).

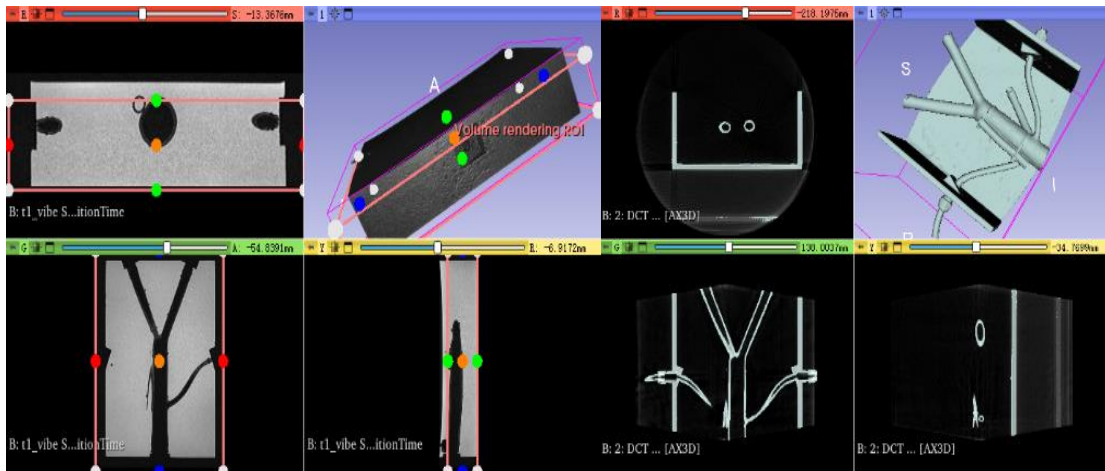


Figure 2.13 Comparison of MRI (left 4) and CT imaging (right 4).

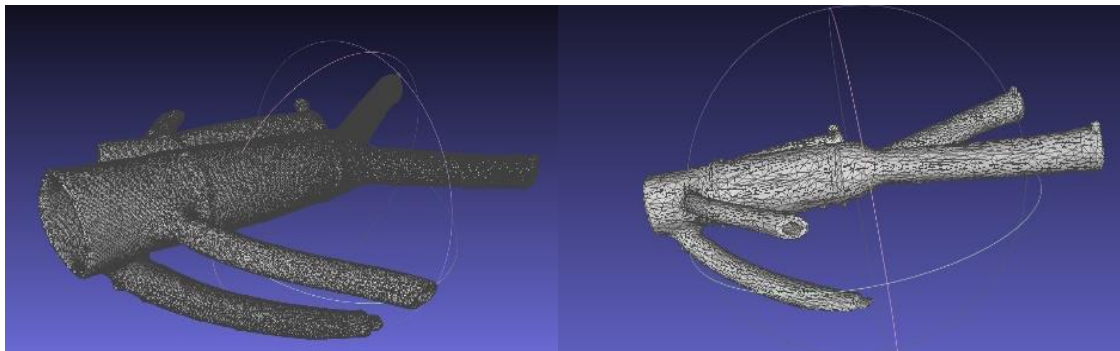


Figure2.14 Left: mesh before processing (221496 vertices 443004faces) Right: mesh after processing (6898 vetices,13836 faces).

2.3.2 Rigid surface model and volume deformation model of phantom in SOFA frame work

When simulating the physics of an object, its topology must therefore be loaded. Before

load the mesh topology into SOFA framework, the position of the model must be located and the size of the model must be specified. Thus, based on the measurement results in Figure 2.3 and the size of the grid in MeshLab, the mesh of phantom model was translated rotated and scaled, and the origin and regular coordinate system were established based on the position of the exit of the abdominal aorta and its center line.

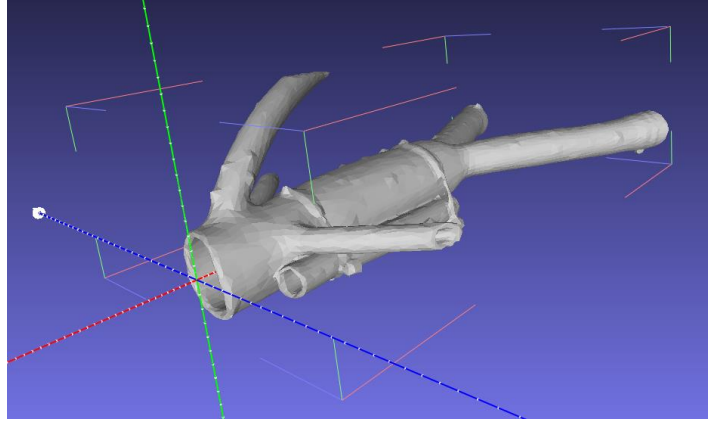


Figure 2.15 Relocation of phantom model in MeshLab.

Since the deformation of the phantom model is very small during the actual insertion of the catheter, it is initially assumed that the model is not deformed, and the topology of the phantom model will not change, that is, the surface mesh model is regarded as an immovable rigid body in the simulation (see figure2.15).

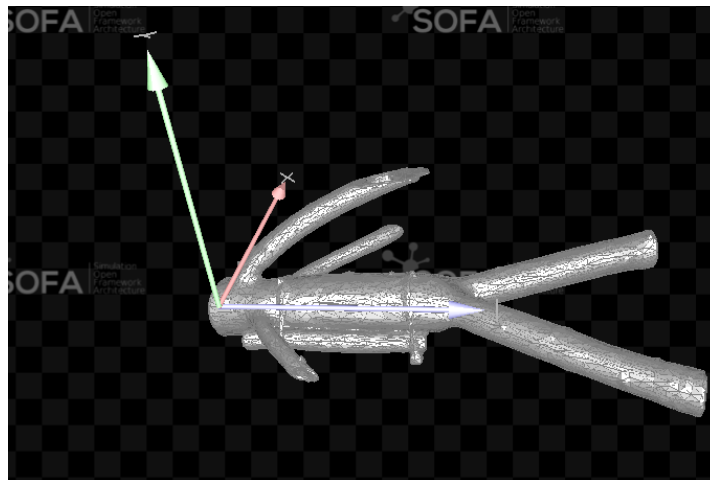


Figure 2.16 Rigid mode in SOFA.

But for more accurate simulation, an elastic model of phantom model is necessary. To this end, it is necessary to generate volume mesh based on phantom surface mesh, and define its deformation method.

Volume mesh generation from surface mesh can be easily realized in Gmsh. Before doing this, the surface mesh file (.stl) needs to be processed in MeshLab to repair non manifold edge by removing faces to fix the non-manifold edge before closing holes using filter *Cleaning and Repairing* and to delete self-intersecting faces by using filters *Close Holes*. Then

import the surface mesh to Gmsh and the volume mesh which contains 1,714 vertices and 8738 cells(tetrahedrons) has been exported using the function *volume generator* (see figure 2.17).

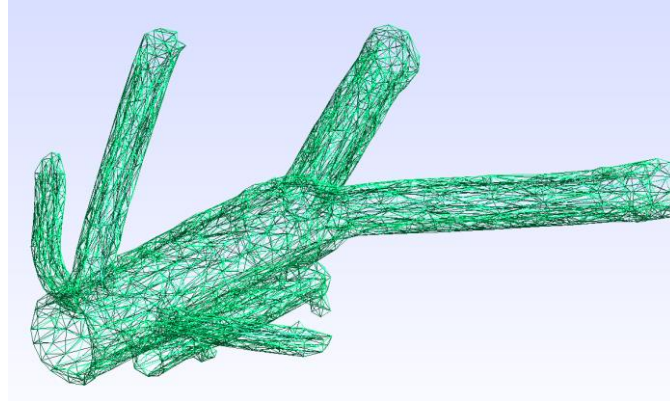


Figure 2.17 Volume mode with tetrahedrons cells in Gmsh.

In SOFA framework, a component *TetrahedronFEMForceField* can be offered for tetrahedral topology to simulate the deformation of this model. It uses FEM to treat each grid cell (tetrahedron) as an elastic unit by defining its Young's modulus and Poisson's ratio. And use the corotational formulation to calculate the stiffness matrix to simulate the deformation of elastic objects. (see Figure2.18)

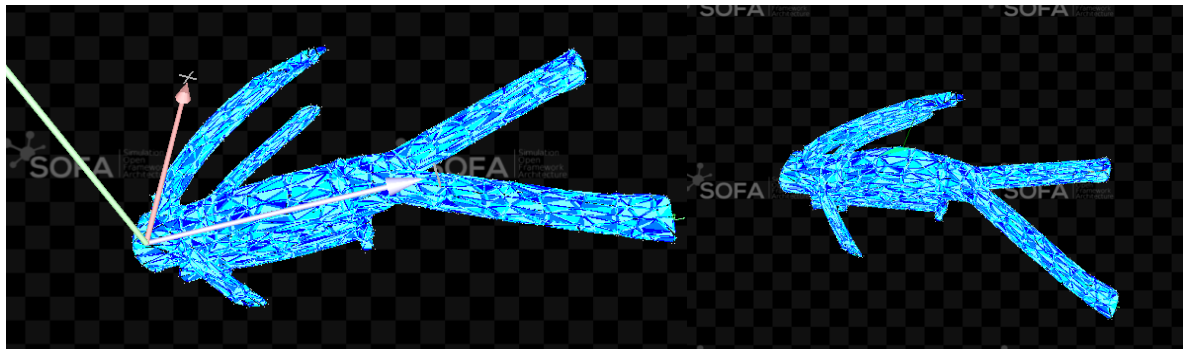


Figure2.18: right: The deformation of the model when a force is applied to a cell surface(green).

2.4 Constraint

In the simulation of the catheter insertion process, there are mainly two types of constraints. One is the fixation of the elastic phantom model, and the other is the constraints caused by the collision between the catheter model and the phantom model.

2.4.1 Fixed constraint of phantom

For the fixation of the phantom model, the method of Projective constraint is adopted. For the fixation of the phantom model, the method of Projective constraint is adopted.

A projection matrix noted P multiplies the matrix A (System matrix) of the linear system $Ax = b$ (where our unknown x is actually evolution of the first derivative Δv) to enforce the so-called project constraint. The system thus becomes:

$$P^T A P \Delta v = P^T b \quad (2.11)$$

This projection matrix P is the identity matrix in which the diagonal value corresponding to the indices of the fixed points equals zero. These lines and columns equal 0. Example of a system of size 4, with a fixed constraint at the indices 3:

$$P = \begin{bmatrix} 1 & 0 & 0 & 0 \\ 0 & 1 & 0 & 0 \\ 0 & 0 & 0 & 0 \\ 0 & 0 & 0 & 1 \end{bmatrix} \quad (2.12)$$

Therefore, based on the phantom mesh model, we find the vertices' indices that need to be fixed and add the fixed constraints (see figure 2.19). As section 1.2, the parts that need to be fixed are 5 area, where the abdominal aorta, iliac arteries and the renal arteries connect to the box.

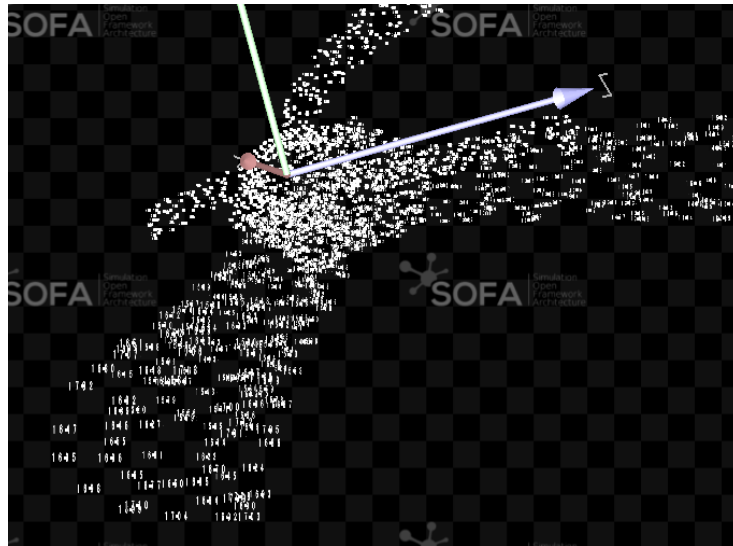


Figure 2.19 Model with numbered vertices in SOFA.

2.4.2 Contact constraint

The flow and viscosity of the liquid are not considered in this simulation. The fluid simulation method Smoothed Particle Hydrodynamics (SPH) models is also provided in SOFA. In future research, the simulation of blood flow can be added to simulate a more realistic environment. Thus, the boundary conditions are represented by the vessel wall and the contacts with the catheter.

a) Contact detection

Before calculate the contact, potential contacts need to be detected first. In this case, we use a *LocalMinDistance* method (which has been integrated into SOFA framework) to detect contact when two objects are getting closer from another. This proximity method detects a

possible contact as soon as pair of collision elements are close to each other (distance smaller than the *alarmDistance*) and will keep only the contacts with the local minimal distance. Then creates contact (aka *DetectionOutput*) when the distance is lower than *contactDistance*.

The detection of the contacts for Object 1 due to an Object 2 is described in figure 2.20:

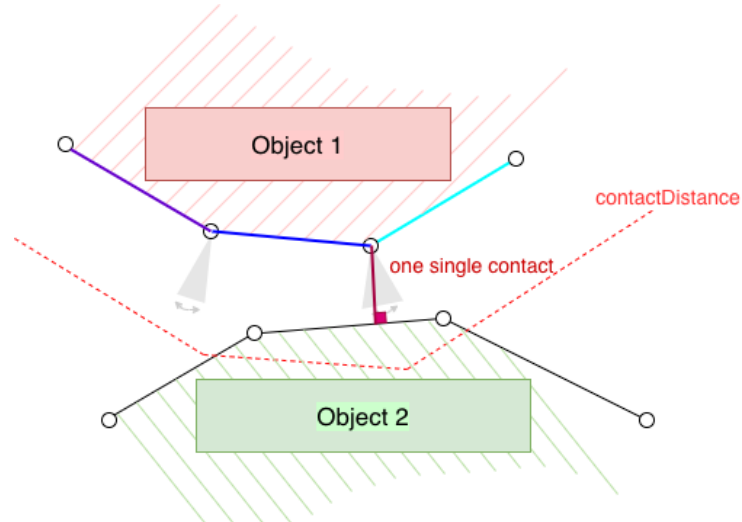


Figure 2.20 *LocalMinDistance* method.

To find an optimal number of contact points, the *LocalMinDistance* computes cones on all nodes of the collision model. A cone is the combination of the orthogonal directions/planes of the neighboring lines/surfaces. All contact outputs which are outside these cones will be invalidated (even if they are below the *contactDistance*). Thus, only the geometrically closest contacts remain: for convex surfaces, this method even ensures to find one and only one contact point.

b) Contact response

Based on above method, the closest point on the surface for each node will be detected. And the direction of interior normal to the surface at this point will be gathered in J . In particular, the Jacobian transpose $J^T = \frac{\partial W}{\partial x}$, represent the linearization of the contact constraints. (See from figure 2.21)

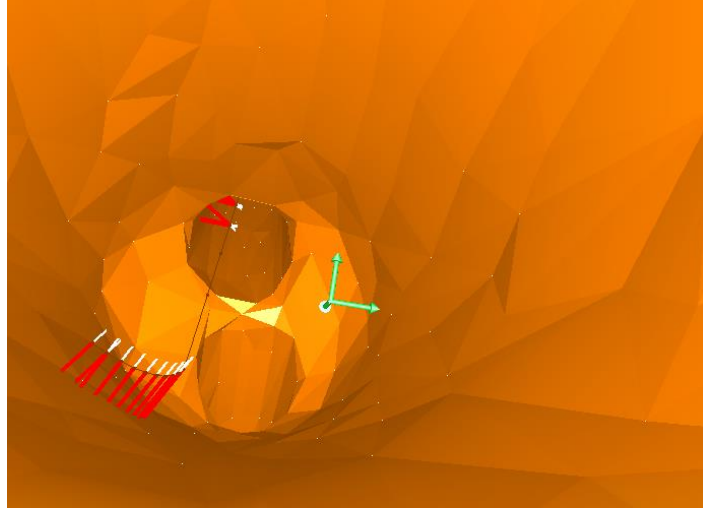


Figure 2.21 Simulation in SOFA: red lines represent the distance from contactDistance (already less than alarmDistance), and the white line indicates normal to the surface.

After potential contact detection, first it is necessary to determine whether the contact occurs, and secondly, it is necessary to define the response method of contact and the impact of contact.

For tissue-tool interactions, most approaches rely on a simple contact model, and rarely account for friction. While this simple action can produce plausible results sometime, but in this case, since there is no liquid inside the phantom, and the material is not smooth, if friction is not considered the result will be an incorrect approximation. Thus, a contact model was built based on the following two laws: Signorini law and Coulomb friction law[33].

The goal of the Signorini law is to prevent penetrations. Given two contact points, it ideally ensures the existing penetration (if any) will be corrected and the existing penetration (if any) will be corrected. Its expression is as follows:

$$\begin{cases} \delta_n \geq 0 \\ \lambda_n \geq 0 \\ \delta_n \lambda_n = 0 \end{cases} \quad (2.13)$$

Where δ_n represent distance between contacts (in normal direction), λ_n represent the force applied on contact point (in normal direction). This means that either the distance between contact bodies is non-negative (no penetration), and a distance of zero indicates contact activation; or the contact pressure between contact bodies is non-negative (no pull and compression), and a pressure of zero indicates contact inactivation. And at the same position, either the contact pressure is zero (contact is not active), or the contact distance is zero (contact is active).

Considering that the contact surface is not smooth, Coulomb friction law defines the tangential contact response due to friction. Its expression is as follows:

$$\lambda_T = -\mu \|\lambda_n\| \frac{\delta_t}{\|\delta_t\|} \quad (2.14)$$

Where μ represents friction parameter which depends on material properties of two objects in contact with each other.

2.4.3 Constraint-based solution (Lagrange multipliers)

To solve the dynamic of two constrained objects, we use a Lagrange Multipliers approach and a single linearization by time step. From the formular(2.9)the constraint problem can be written in a simpler way as:

$$A\Delta v = b + dtJ^T\lambda \quad (2.15)$$

Where $J^T\lambda$ is the vector of constraint forces contribution with J containing the constraint directions and λ are the so-called Lagrange multipliers.

For each constraint, a constraint law is assigned, which depends on the relative position of the interacting objects:

$$\Psi(x_1, x_2 \dots) \geq 0 \quad (2.16)$$

Ψ represents unilateral interaction law (Signorini- Coulomb model).

In the constrained system presented above, the constraint matrix J appeared. The definition of the constraint laws allows to define:

$$J_1(x) = \frac{\partial \Psi}{\partial x_1} \quad (2.17)$$

$$J_2(x) = \frac{\partial \Psi}{\partial x_2} \quad (2.18)$$

Note that the matrix J containing the constraint directions can be considered as the Jacobian of the mapping between the physics space and the constraint space. For two interacting objects (object 1 and object 2), the complete constrained system therefore corresponds to:

$$A_1\Delta v_1 = b_1 + dtJ_1^T\lambda \quad (2.19)$$

$$A_2\Delta v_2 = b_2 + dtJ_2^T\lambda \quad (2.20)$$

In SOFA framework, this system is solved in two steps:

Each interacting object is solved independently [34], i.e., as no constraint law is defined, while setting Lagrange multipliers. This so-called free motion aims at finding the change in velocity

Δv_1^{free} and Δv_2^{free} for each object from the resolution of:

$$A_1\Delta v_1^{free} = b_1 \quad (2.21)$$

$$A_2\Delta v_2^{free} = b_2 \quad (2.22)$$

Then, the constraints are taken into account while considering $b_1 = b_2 = 0$ to look for a corrective change in velocity Δv_1^{corr} and Δv_2^{corr} for each object from the resolution of:

$$A_1\Delta v_1^{corr} = dtJ_1^T\lambda \quad (2.23)$$

$$A_2\Delta v_2^{corr} = dtJ_2^T\lambda \quad (2.24)$$

Defining λ the Lagrange multipliers, as the forces to be applied in the constraint space to satisfy all constraint laws, the constrained system can therefore be presented as:

$$\delta = J_1 v_1^{free} - J_2 v_2^{free} + dt [J_1 A_1^{-1} J_1^T + J_2 A_2^{-1} J_2^T] \lambda \quad (2.25)$$

Where $[J_1 A_1^{-1} J_1^T + J_2 A_2^{-1} J_2^T]$ represent the matrix of constraint system, δ is the constraint violation (δ is the distance the interpenetration, projected along the constraint directions.)

Finally, the resolution of the constraint problem is done using the Gauss-Seidel algorithm [34]. After resolution of this new linear system, the motion can be corrected as follows:

$$x_1 = x_1^{free} + dt \Delta v_1^{corr}, \quad \Delta v_1^{corr} = dt A_1^{-1} J_1 \lambda \quad (2.26)$$

$$x_2 = x_2^{free} + dt \Delta v_2^{corr}, \quad \Delta v_2^{corr} = dt A_2^{-1} J_2 \lambda \quad (2.27)$$

3. Experiment and Result

In the following, the process of catheter insertion from the left iliac artery into the abdominal aorta is simulated in sofa framework. The simulation setup is described in section 3.1. And an experiment (section 3.2) is set up to evaluate the contact forces and catheter position information estimated from the simulation results. In the experiment, the contact forces are obtained by the force sensor, and the position information is obtained by the image-based method (section 3.3).

3.1 Simulation setting

The simulation is based on the following scenario (see figure 3.1): a catheter with a pre-curved tip is inserted at a constant velocity from the left iliac arteries-box interface into the phantom (with 5 parts fixed to the box).

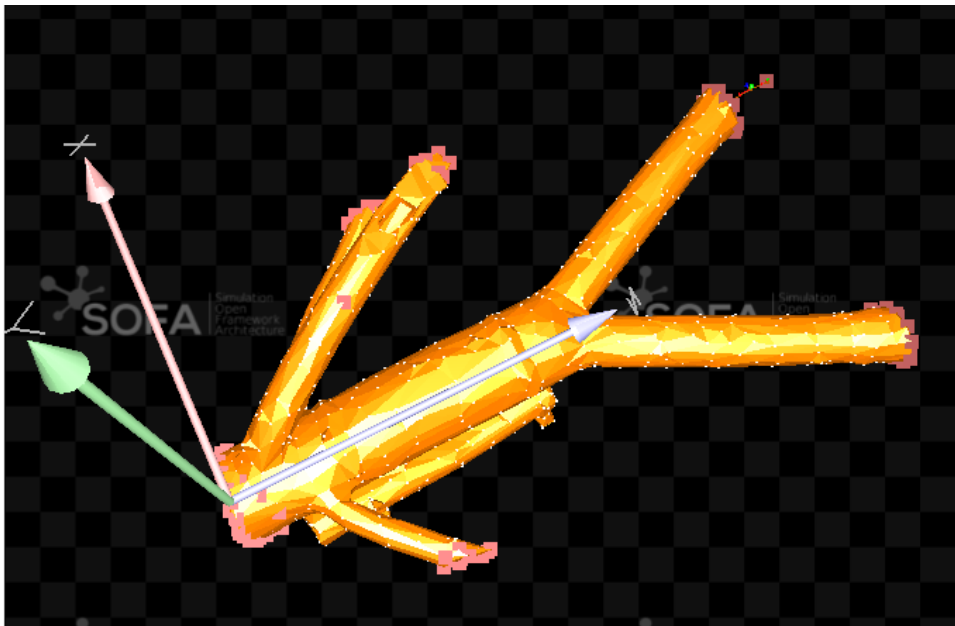


Figure 3.1: Simulation scenario: The yellow part is the phantom model, the pink points are fixed constraints imposed on it, and the red line is the inserted catheter.

As mentioned in Section 4.1, the model of the catheter is realized by a plugin *beamAdapter* [26] in the SOFA framework. The plugin *beamAdapter* in SOFA framework implements a 1-dimensional Finite Element Method (FEM) in the context of coil embolization in neurology. The method is based on Timoshenko beam theory, and allows to simulate any 1D flexible structure, like catheters or guidewires with options to set parameters in *wireRestShape* module to realize the deformation simulation of the model.

In this work, Impress® Diagnostic Peripheral Catheter [26] were used and we assume that mechanical parameters, such as Young's modulus [35], mass Density, length or tip form (simply as a semicircle), can be determined either from literature or through simple measurements and define them as ground truth. And a simple experiment has been set to observe the effect of model mechanical properties by change several parameter settings.

In addition to the above parameters, since in the FEM model, the catheter is composed of a large number of beam elements (each containing two 6-DoF nodes), by changing the number of nodes, the accuracy and speed of the simulation will also be affected. Table 3.1 records the different parameter settings in the plugin.

	Ground truth	M 1	M 2	M3	M4	M 5	M 6	M 7	M8
Straight Length [mm]	800	800	800	800	800	800	800	800	800
Total length [mm]	825	825	825	825	825	825	825	825	825
spire Diameter(tip) [mm]	16	16	16	16	16	16	16	16	16
Young's Modulus (proximal) [GPa]	600	600	600	600	300	200	600	800	600
Material - Density [g / mm^3]	1.55	1.55	1.55	1.55	1.55	1.55	4	1.55	1
Number of nodes(distal)	50	10	25	70	50	50	50	50	50

Table 3.1. Catheter setup parameters to use with *BeamAdapter* plugin

By setting up new scene simulation scene, fix the end of the catheter, apply gravity to the catheter, and compare the influence of the selection of different Young's modulus, material - density, and number of nodes on the catheter model. (And compare it to the actual

curve of catheter, note: The actual curve is inherently curved due to long-term use. Its deformation and stored energy can lead to errors in position and force estimation).

And for phantom model, we assume the Young's modulus 2.7 (MPa) and Poisson Ratio 0.4[36]be the ground truth.

From section 2.3.2, friction coefficient μ will also influence the results of simulation due to contact but it is hard to measure the friction coefficient between the inner surface of the phantom model and the catheter. As ground truth value, the friction coefficient was set according to literature [37] to 0.62. And as above, change this parameter to observe its impact on the result(figure).

As mentioned in section2.3.2, in simulation, we rely on the Lagrange Multiplier method to solve the constraints using a Gauss Seidel. This means that the contact forces will exist in the form of each constraint. In order to obtain the contact force on the entire catheter at a certain moment, it is necessary to derive the resultant force of the constraint force generated by each constraint activation on each node in each time step, which can be obtained by summing the forces constrained on each node. And the torque can be obtained by combining the position of the node and the force acting on this node.

$$F_{sum} = \sum F_i \quad (3.1)$$

$$M = \sum L_i \times F_i \quad (3.2)$$

Where F_i represents force on node i , L_i represents the position vector of node i .

In SOFA framework, constraint force will be stored as the following form:

$$[constraintID, number\ of\ Constraint, nodeID, normal\ direction] \quad (3.3)$$

$$F_i[nodeID] += Deriv(constraintID) * \lambda[constraintID] \quad (3.4)$$

Where lambda multiplier λ resulting from the Gauss Seidel resolution.

Thus, a python script is written to read and output the positions, forces and moments at the end of each time step. Data processing and visualization are done in MATLAB. In the simulation in the sofa framework, the contact force will be displayed as a white line. (figure3.2)

3.2 Catheter insertion &force measurement

In order to realize the process of inserting the catheter at a fixed point and at a constant speed in the simulation scene, the Cathbot is prepared to be used at the beginning. The slave robot is controlled to insert the catheter at a constant speed through the master device. However, since the slave robot is currently unavailable, the simplified device in the figure below is adopted to complete the process(figure3.3).

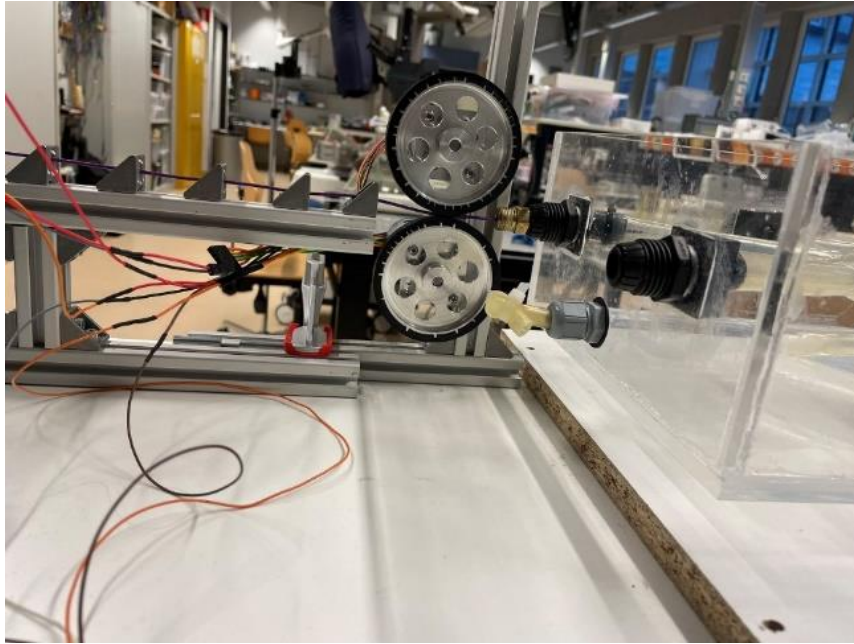


Figure 3.3 Alternative device to insert the catheter.

Catheter insertion movement is accomplished by friction with two counter-rotating squeezed wheels. The wheels are driven by two identical motors (Servo city Premium Planetary Gear Motor). Due to the small load, the speed of the motor can be roughly controlled by setting a constant voltage to keep constant, and the friction force between the wheel and the surface of the catheter can be increased by loading the rubber layer on the wheel. Assuming that there is no sliding friction between the wheel and the surface of the catheter, the linear velocity of the wheel rotation can be approximated as the insertion speed of the catheter. The speed of the wheel can be calculated from the frequency of the output signal of the motor encoder. And in order to ensure the insertion direction, a catheter stopper is set before and after the feeding device.

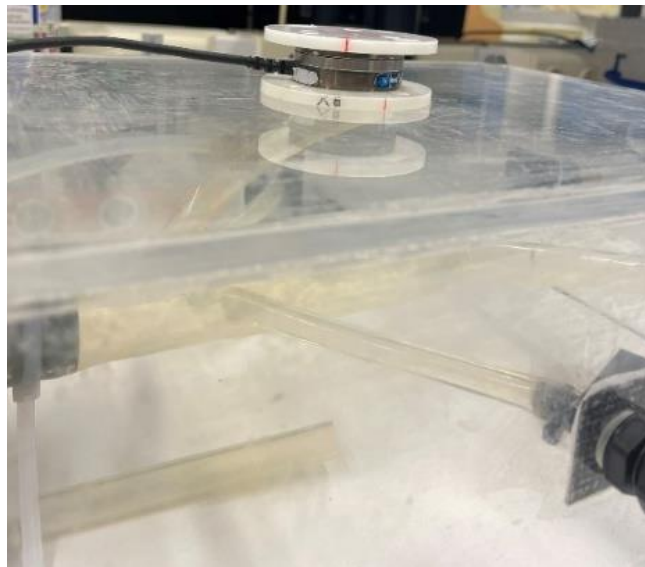


Figure 3.4 Fixed force sensor.

During the insertion process, the force and torque data on the phantom are obtained by the sensor ATI mini-40 force torque sensor. This sensor can be used to measure forces in all 3 axis (up to 80 N for F_x and F_y , 240 N for F_z) and torques in all three axes as well (up to 4 Nm all axis). Data collection is realized through its own software Net F/T Demo software. The "Net F/T demo" software allows the user to view the forces and torques acting upon the sensor in real time, save sensor values to file, log sensor values (sampling rate is 1000hz) and zero the sensor values. Data processing and visualization are done in MATLAB.

3.3 Configuration extraction

Since the method using sensor on catheter will change the physical parameters of the device, which will result in the deviation of the simulation results. So, in this work, the image method is used to collect the position and configuration information of the catheter during the experiment. The original plan for the project was to use X-ray imaging to obtain images of catheters with X-ray opaque coating in two views. Since the position information of the catheter cannot be obtained due to too much occlusion in the side view, and to simplify the experimental setup in this work, we use RGB images with single view as an alternative method.

During the insertion of the catheter, fix a webcam (model Logitech C920) above the phantom box to obtain real-time images, the image resolution is 1280*720, and the frame rate is 30HZ Select one frame per second in the obtained video for the next comparison work. Since there is no side view and the diameter of the blood vessel is small, it is assumed that the pose of the catheter obtained from the top view is located on the plane of the centerline of the blood vessel. To map the catheter position points in the image coordinates to points in the world coordinates, we need to compute the rotation and the translation of the camera relative to the calibrated plane coordinates i.e., camera calibration. In this work, the camera is calibrated based on Zhang's camera calibration algorithm [38] using MATLAB. The following steps are all done with the camera fixed and the focal length unchanged:

1. Take multiple images of a calibration pattern (asymmetric checkerboard) from different angles;
2. Detect the checkerboard corners in the images to estimate Camera Parameters (intrinsic parameters and extrinsic parameters), and use reprojection error to evaluate the calibration accuracy (see figure 3.6 left). The bar graph indicates the accuracy of the calibration. Each bar shows the mean reprojection error for the corresponding calibration image. The reprojection errors are the distances between the corner points detected in the image, and the corresponding ideal world points projected into the image;
3. Use the camera intrinsic parameters to remove lens distortion from the image (see figure3.6 right), which is necessary for accurate measurement;
4. Manual extraction of catheter positions from undistorted Image (see figure3.7). For the tip, three points are evenly extracted as the tip position, and points are also extracted at equal intervals for the remaining proximal parts;

5. Eliminate the lens distortion of the calibration pattern image on the same plane as the catheter, and use the distorted image to calculate new camera extrinsic parameters (translation and rotation matrices). Using these parameters maps undistorted image points, onto points on the X-Z plane in world coordinates (Use the function *img2world2d* in MATLAB to complete), see figure 3.8;
6. The three points of the tip will be used to compare with the tip position of the simulation results; Bezier curve [39] are used to fit the points of the proximal part to get a smoother curve to compare with the simulation results (see figure 3.9).

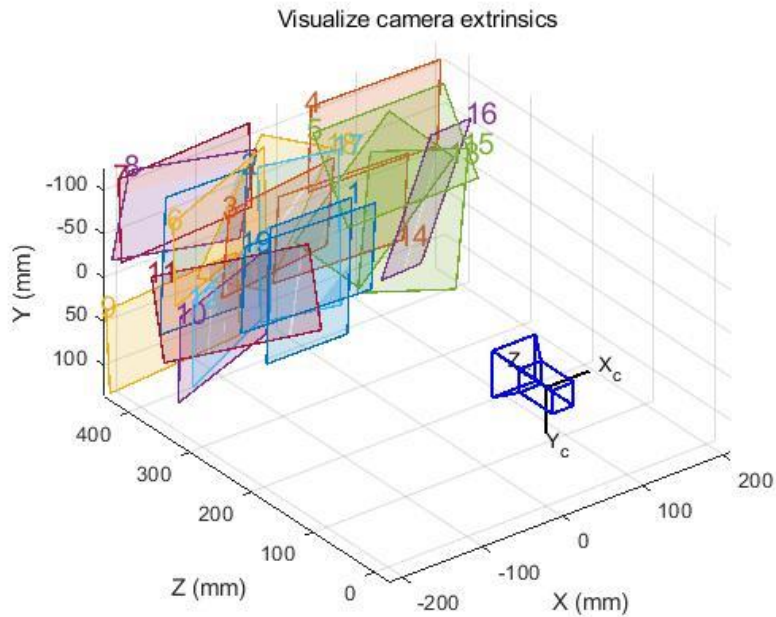


Figure 3.6 Visualized camera extrinsic parameters of calibration pattern with different position.

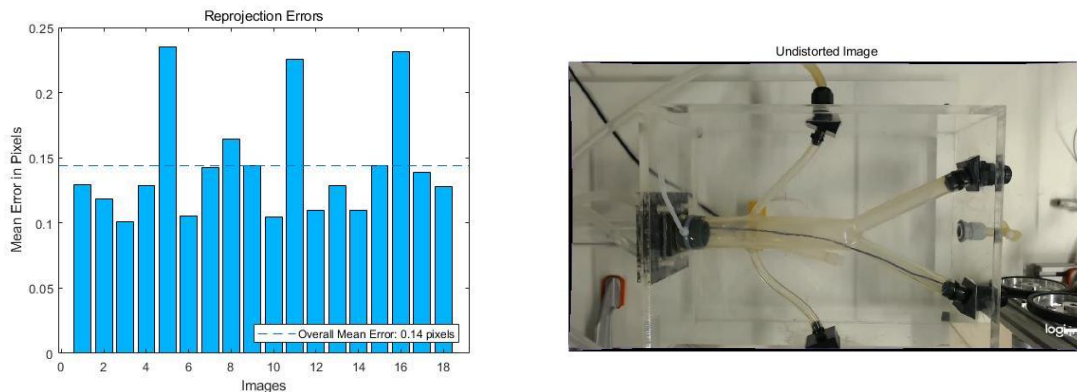


Figure 3.6 Camera calibration.

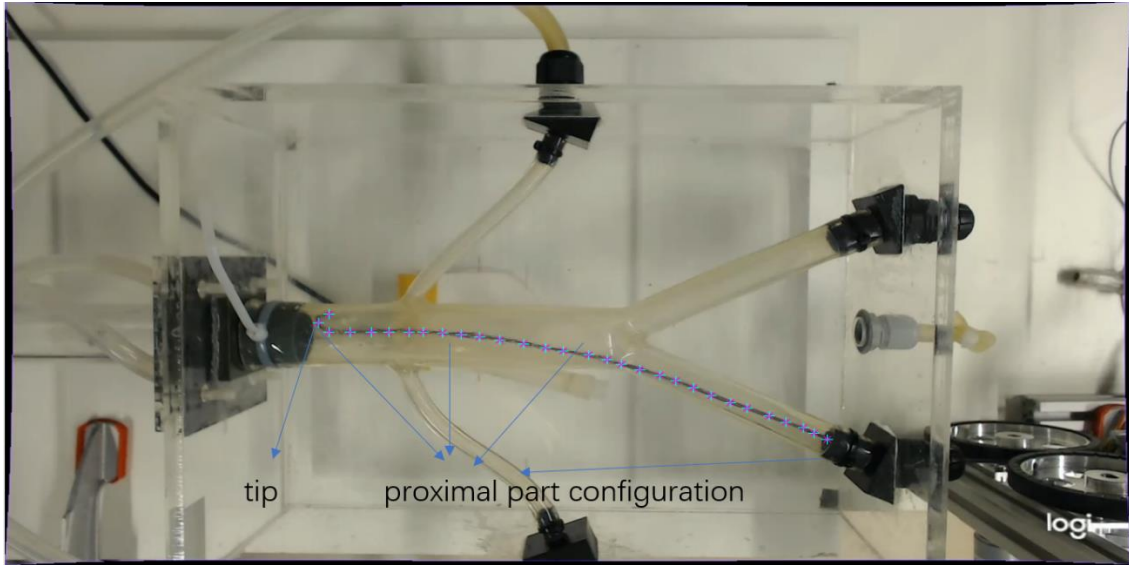
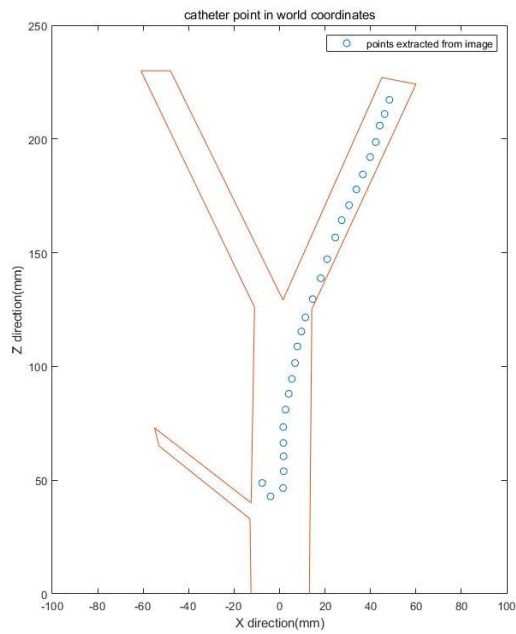


Figure 3.7 Manual extraction of catheter positions.



. Figure 3.8 Points extracted from image in world coordinate.

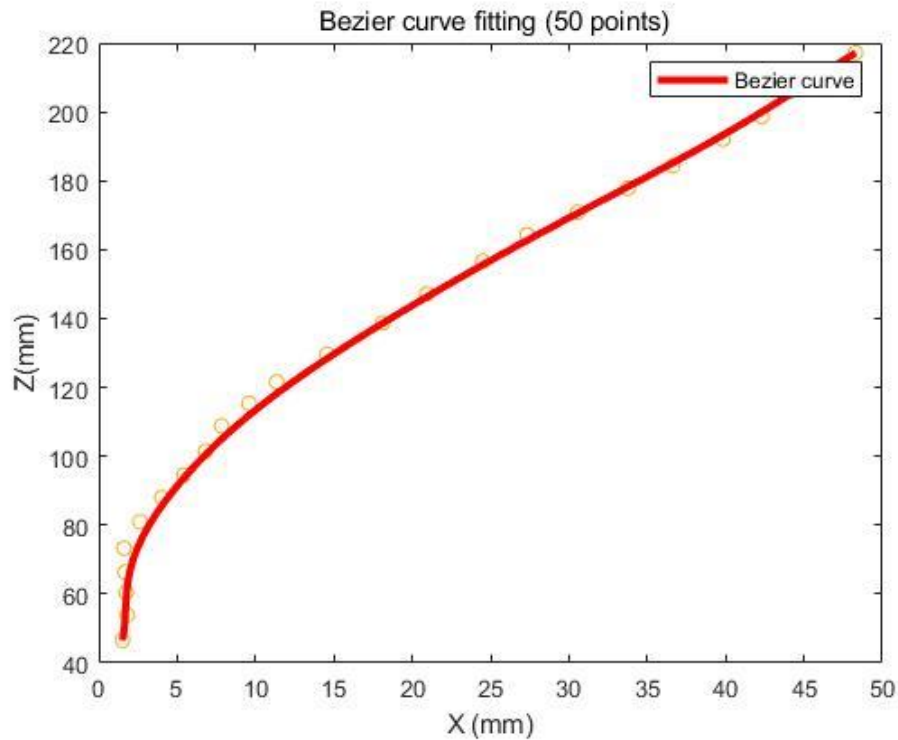


Figure 3.9 Bezier curve fitting.

3.4 Results and discussion

In section 3.1, simulation and experimental results are presented. After some noise reduction processing on the experimental results, they were compared with the simulation results. The results of position and contact forces estimation are discussed in section 3.2.

3.4.1 Results

Based on the data in Table 3.1, we can get the catheter configuration in the gravity environment as shown in figure 3.10 3.11. 3.12.

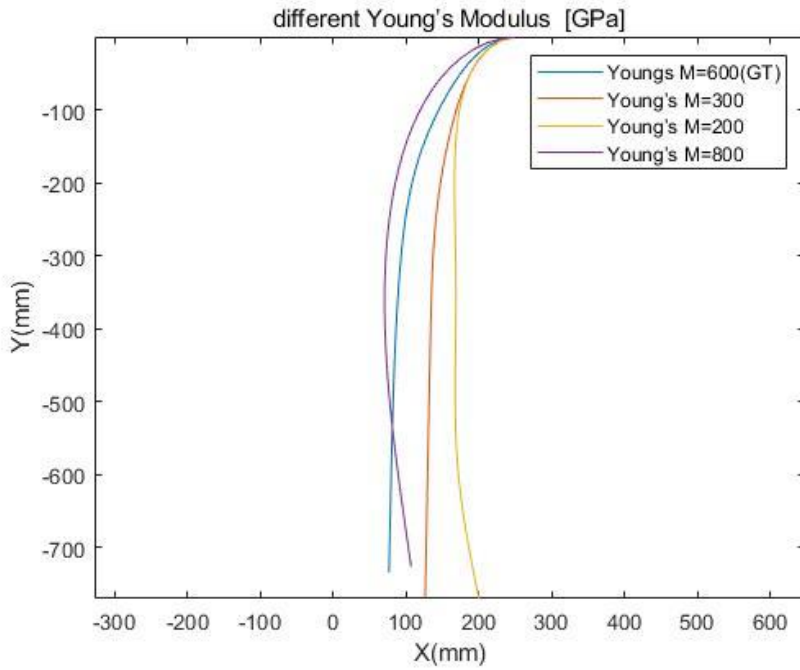


Figure 3.10 Catheter model configuration using different Young's Modulus.

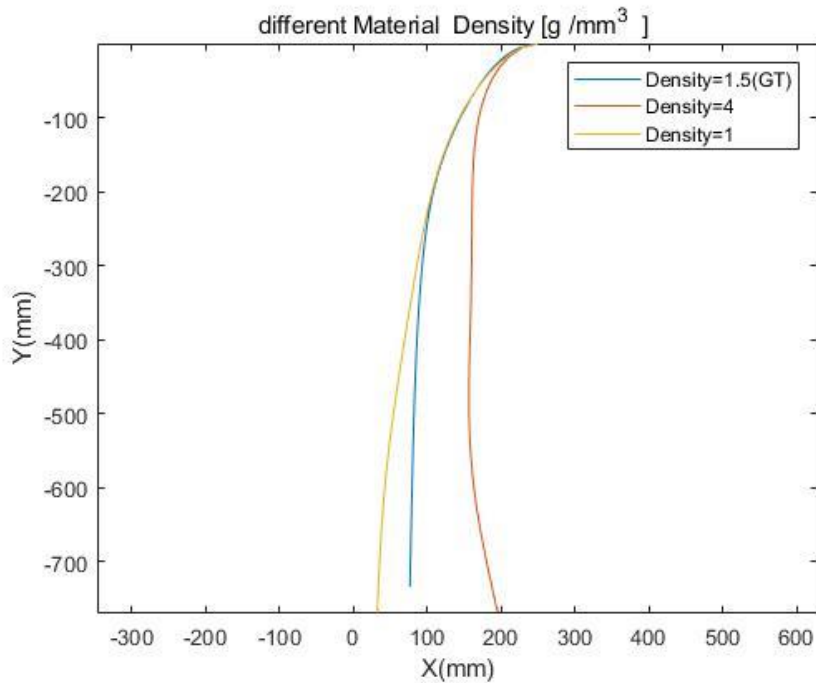


Figure 3.11 Catheter model configuration using different Mass density.

It can be seen from the above that the influence of physical parameters on the model state is very obvious. By looking at the error distance, since the inner diameter of the blood vessels in the phantom model is small, these parameters should be set based on accurate measurements or by consulting the literature.

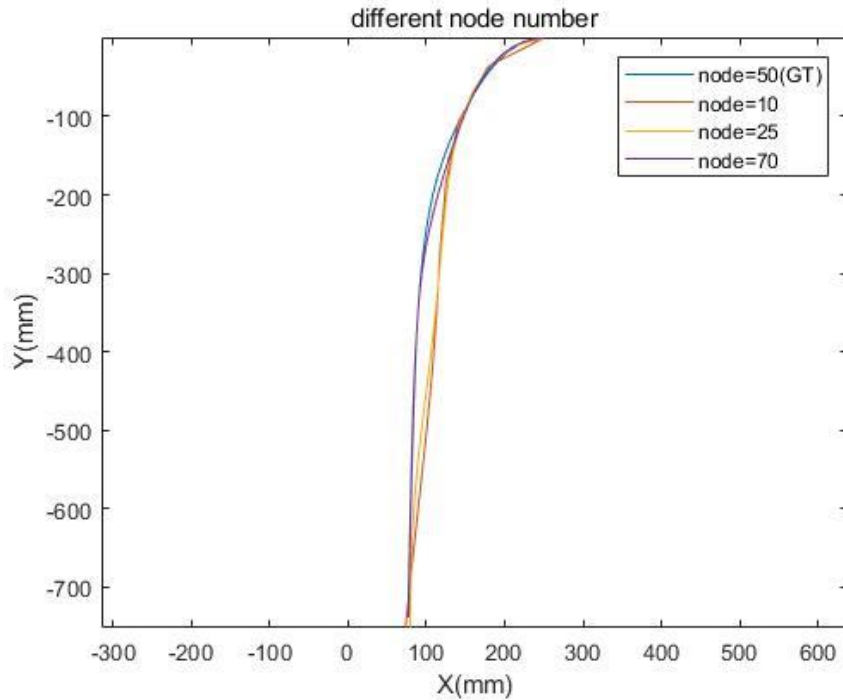


Figure 3.12 Catheter model configuration using different numbers of nodes.

For different numbers of nodes (see figure 3.12), we found that reducing the number will make the model inaccurate, but the simulation speed will increase. On the contrary, increasing the number of nodes will reduce the simulation speed and increase the simulation accuracy. But when the number is large enough (50), if increase the number of nodes, the simulation results will get closer and closer, but the speed will be significantly reduced. Therefore, choosing a reasonable number of nodes can balance the relationship between simulation accuracy and simulation speed.

For the insertion process of the catheter, two feed speeds are applied in the simulation and the practical experiment, 13mm/s and 23mm/s . However, due to the change of the motor load, the speed in the actual experiment is not constant, and there is a deviation of 2mm/s (measured by the frequency of the output signal of the motor encoder). The different results of experiment caused by different speeds are as follows:

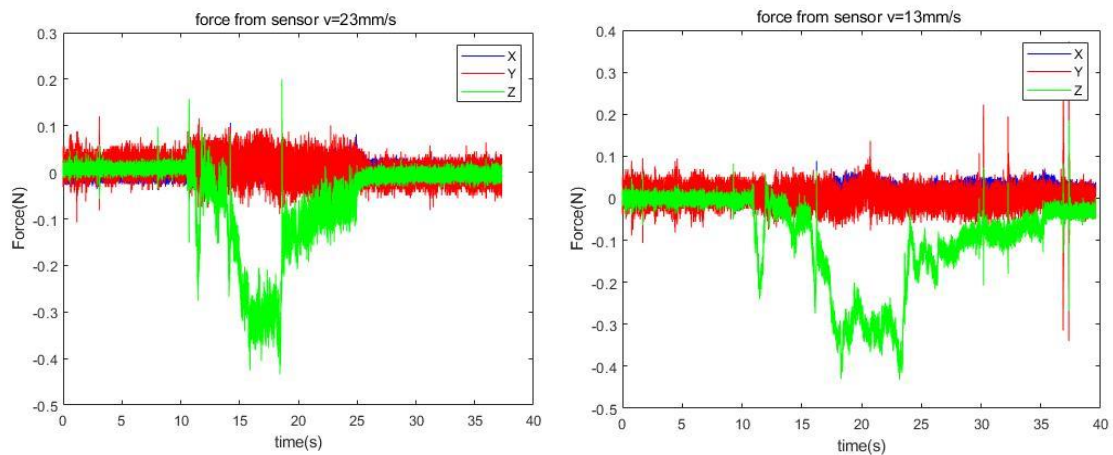


Figure3.13 Force from experiment with different insertion speed.

From the data obtained by the sensor (see figure 3.13), it can be seen that the insertion speed has little effect on the magnitude of the force, but only affects the speed of the catheter contact state. And the force of Y (gravity direction) has little influence on the result, so the following analysis and discussion will only be carried out on the force in the direction of X (perpendicular to the insertion direction on the horizontal plane) and Z (the insertion direction) with insertion speed $v = 13mm/s$.

Furthermore, it can be seen that due to the instability of the speed and the large noise amplitude of the sensor, the measured data is seriously oscillated. Therefore, some denoise algorithms are used to process data. First find and replace the outliers, and use the wavelet noise reduction method to remove some high-frequency noise, and finally, due to the high sampling frequency (1000hz), use the moving average to reduce the periodic trend in the data. The processed sensor data is shown in figure 3.14:

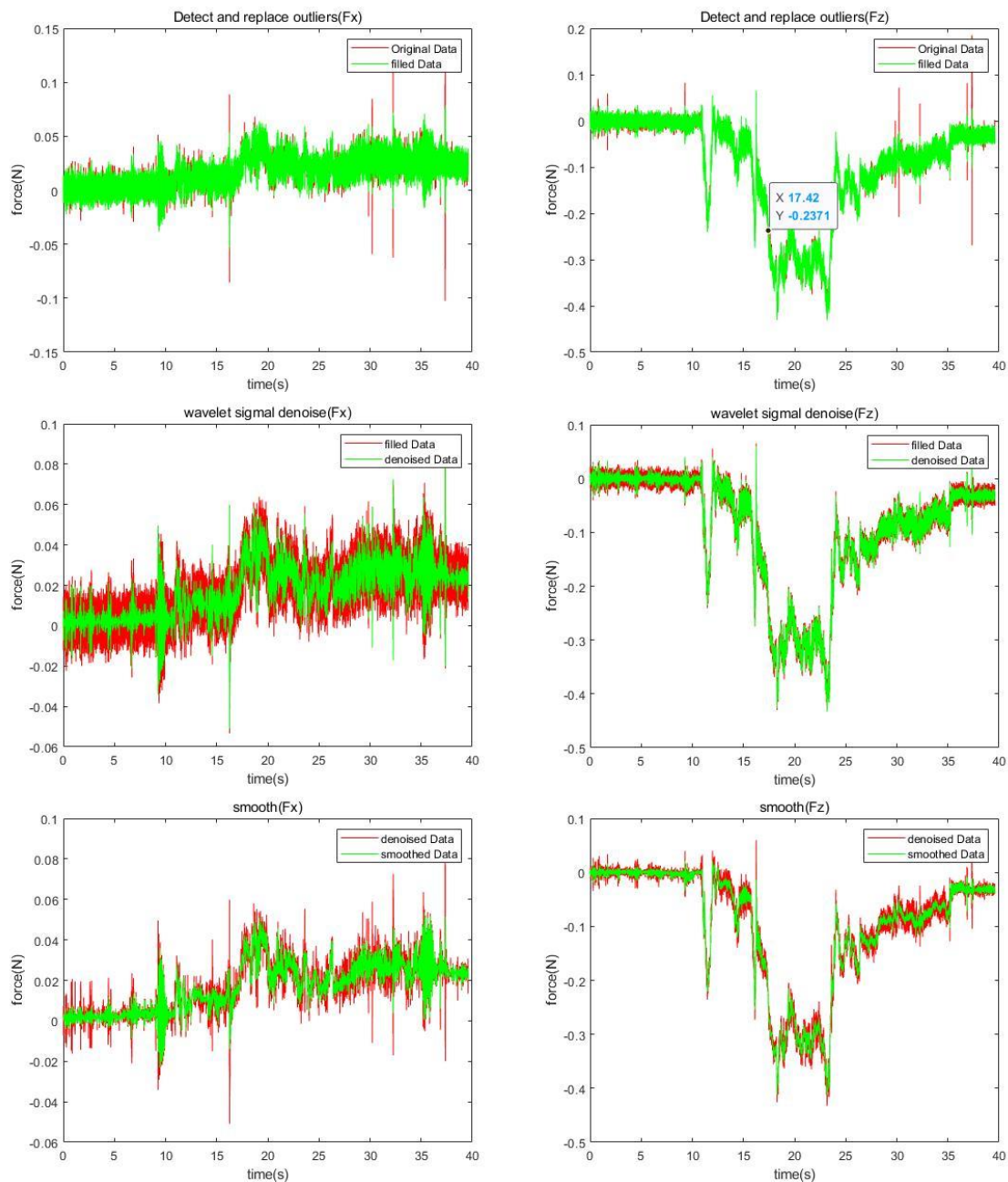


Figure3.14 Sensor data processing (left: X direction; right: Z direction).

Then compare the processed sensor data with the simulation output:

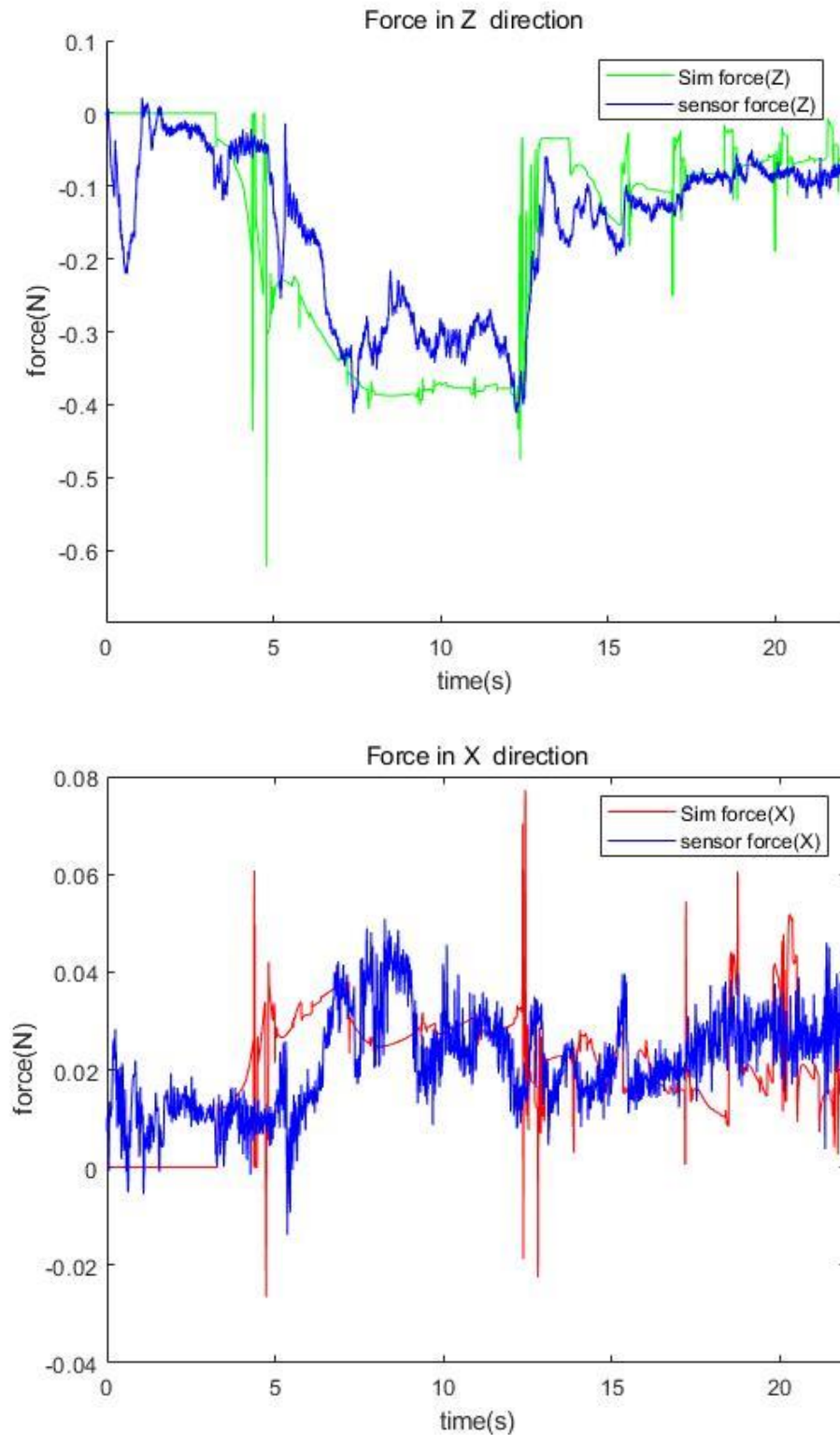


Figure3.15 Comparison of sensor data and simulation output results.

Due to the existence of the direction limit device, the force measured during the insertion of the pre-bent tip into the phantom model in the experiment is much smaller than the force output from simulation (figure 3.15 before 6.1s).

Ignore the error caused by the limit device in the first 6.1s, using the sensor data as a reference value, respectively calculate the absolute error and relative error of the X-direction and Z-direction forces obtained from the simulation results, and calculate the absolute error and relative error of the total forces (see figure 3.16).

Through calculation, the error in the X direction during the insertion process is 0.0058N (24.29%), the Z direction is 0.034N (19.35%), and the error of the total force is 0.0371N (30.45%).

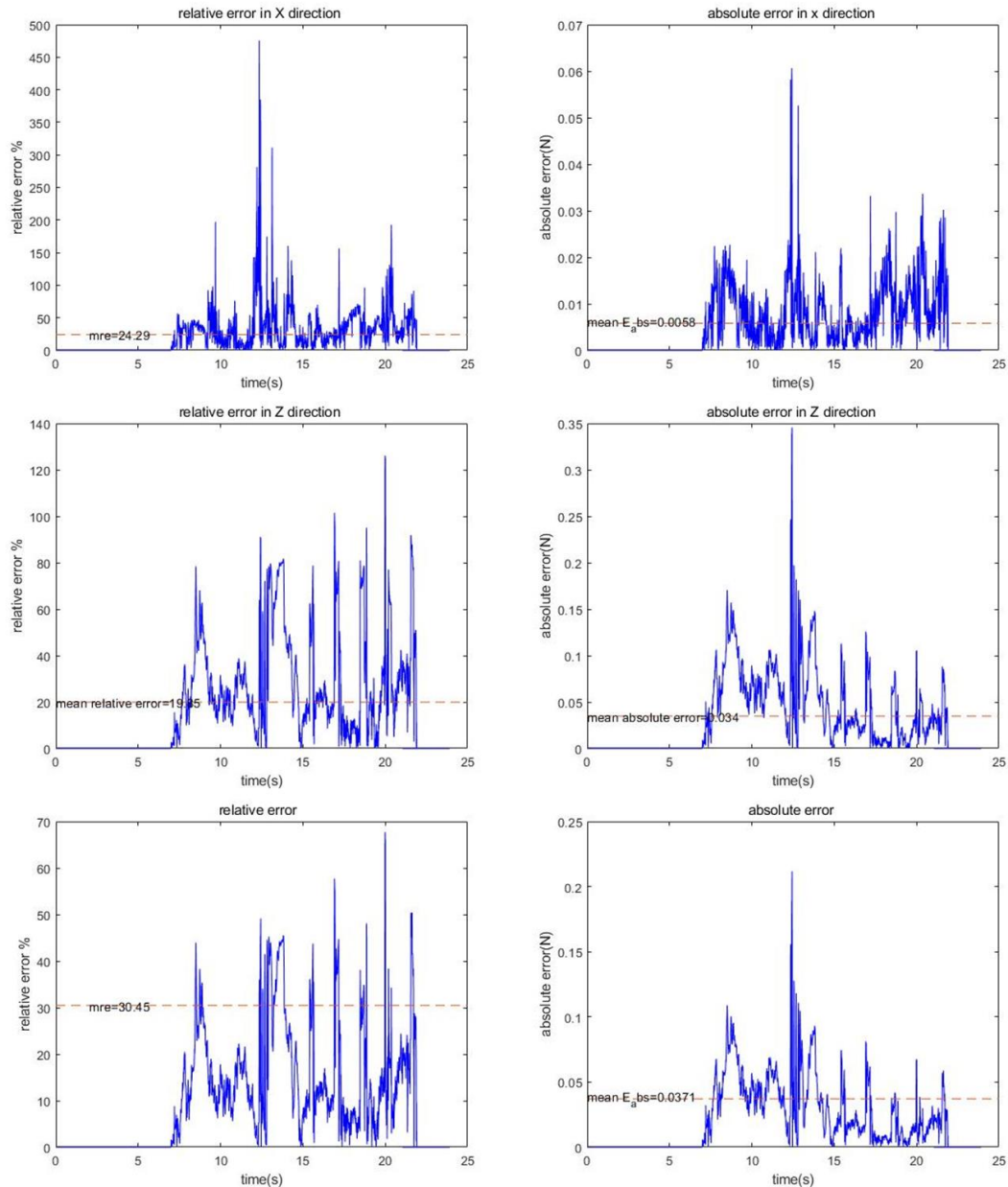


Figure3.16 Comparison of sensor data and simulation output results.

The figure below (figure 3.17) shows the comparison of the position of the catheter tip and the configuration of the proximal part between the outputs from the simulation from images.

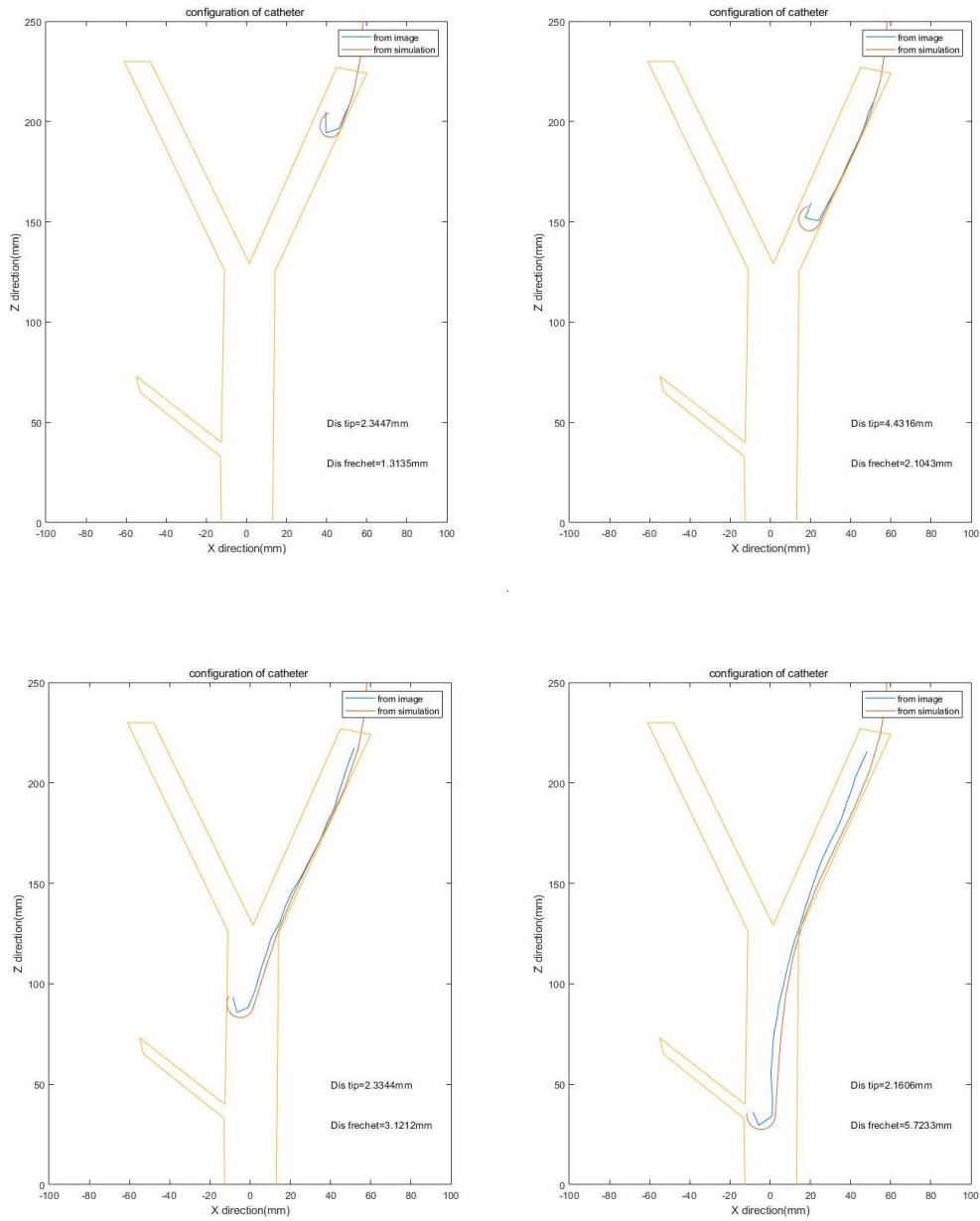


Figure3.17 Position and configuration comparison (time interval=4s).

In order to evaluate the accuracy of the simulation, the distance error of the tip is calculated with the Euler distance, and the Fréchet distance [40] is used to evaluate the similarity of the proximal part curves. After calculation, during the insertion process, the average error of the tip position is 3.1mm, and the mean Fréchet distance of the proximal part is 3.6mm.

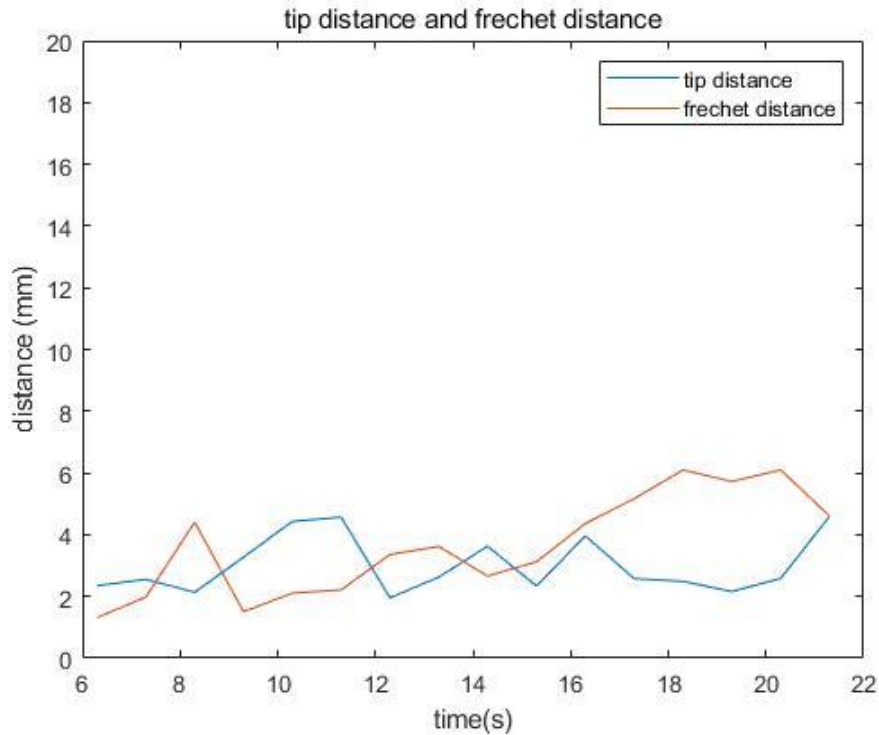


Figure3.18 Error of tip position and proximal part configuration.

3.4.2 Discussion

From the estimation results of the contact force, it can be seen that the force in the process of inserting the catheter without simulated blood flow is much smaller than that in the process of inserting the catheter in the simulated blood flow [10], the main form of forces are collision forces and friction forces with vessel walls.

Due to the existence of the direction limit device, the force measured during the insertion of the pre-bent tip into the phantom model in the experiment is much smaller than the force output from simulation. As the tip enters the iliac arteries, the catheter is primarily affected by friction from contact with the vessel wall. In the case of a friction coefficient of 0.6, the simulation results of this process force are roughly the same as the actual measurement results (Figure3.15).

When the catheter tip passes through the iliac arteries and has not yet reached the abdominal aorta, the measured force will suddenly decrease or even disappear. When the tip touches the abdominal aorta, the force on the catheter will increase significantly (due to collision), A greater insertion speed increases this force but decays rapidly with time. Afterwards, the force on the catheter is mainly the sliding friction force with the wall of the abdominal aorta. Except at the collision of the tip in the above-mentioned stages, since the main form of force on the catheter is sliding friction, the influence of speed changes on it is

not obvious in other time periods. (Figure 3.13).

And from the whole process, the accuracy of the force estimation results in the insertion direction (slightly higher than 80%) is higher than that in other directions (70%), which may be due to the small measurement deviation relative to other directions due to the larger contact force in the insertion direction.

For the estimation of the tip position, it can be seen from Figure 3.18 that the error has been fluctuating around 3.1mm. Combined with the Figure 3.17, this may be caused by the instability of the insertion speed. This result is slightly larger than image-based catheter tip tracking (tip 1.3mm) referred by Ma, H., Smal. etc. in 2020 [41]. But it is more accurate than the result obtained by the method (mean 4.3mm) referred by Ambrosini in 2015 [42] using Image-based 3D reconstruction. And considering the instability of insertion speed, this result is acceptable. For the similarity of the proximal part of the curve, although the Fréchet distance shows a high similarity, it can be seen from Figure 3.18 that the Fréchet distance tends to increase with the increase of the insertion length. Moreover, due to the lack of depth direction information, the error of this part may be larger than the results.

From the above results, it can be seen that the model-based method can simulate the insertion process of the catheter in the phantom model in real time using SOFA framework, and can obtain the contact of the catheter and the configuration of the catheter within an acceptable error range. In the Cathbot, compared with the previous method of obtaining the contact force by detecting the distance between the tip position and the vessel wall, the method based on the model is used to analyze the force situation from a physical perspective, and the results obtained are more realistic. And the generation of contact force not only focuses on the contact of the tip, but also analyzes the overall force of the catheter by combining the configuration of the catheter and the contact form of the phantom model (figure 3.19). This way the contact force is more realistic to the operator of the insertion process.

However, from the results, the accuracy of model-based methods is deeply dependent on the accuracy of model parameters (such as material properties, measurement results), and more accurate measurement methods will have a more positive impact on simulation results.

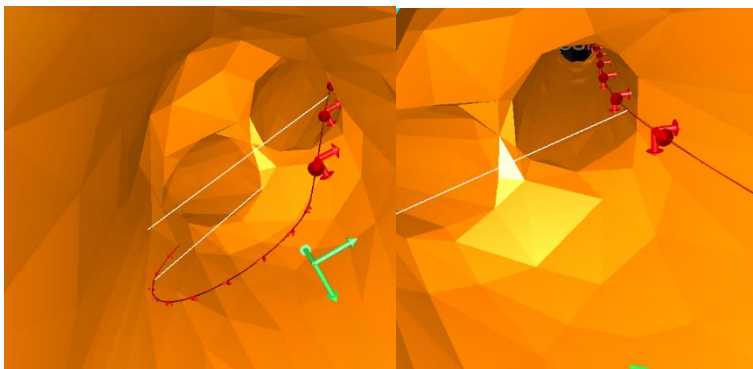


Figure 3.19 Simulation: The white line represents the force on the node when contact occurs

And the calculation of contact recovery in the simulation is based on the normal direction of the contact surface, so the smoothness and fitting accuracy of the surface mesh will have a great impact on the results. How to take into account the real-time and accuracy of the simulation is also a problem that needs attention.

4. Conclusions and Future Directions

4.1 Conclusions

The purpose of this thesis was to build a physical model-based method to simulate the interaction of the catheter and phantom model during insertion of catheter using SOFA framework. Then the force on the catheter due to contact with the phantom model was estimated from the simulation. And hope to improve the haptic feedback system in the Cathbot platform by estimating the force in real-time simulation, so that the feedback force felt by the operator during the operation will be more real. The estimated forces were verified by setting experiments. The experimental results show that by setting reasonable physical simulation parameters, this method can more accurately describe the force of each stage of catheter insertion and with 80% accuracy in the direction of insertion. And the pose of the catheter at each moment can be estimated.

In this paper, the catheter physical model is established based on beam theory, and FEM is used for simulation and the influence of different physical parameters on the simulation results is analyzed. Export a 3D mesh model of phantom was exported from CT DICOM data using 3Dslicer, MeshLab, and Gmsh, and an elastic model was established based on the phantom 3d volume mesh for real-time simulation. In the simulation process, the influence of friction is fully considered, and the finite element model is constrained by combining Signorini law and Coulomb's friction law. The constraint problem is solved using Lagrange multiplier method. And for force estimation, not only the force on the tip of the catheter but all the contact points on the total length of the catheter are considered.

However, the accuracy of this method needs to be based on the accuracy of the physical model, not only for the physical characteristics of the catheter and phantom, but also for its interaction with the environment and noise. More accurate physical model information will lead to more accurate simulation results.

4.2 Open Challenges and Future Directions

In this work, both experimental and simulation scenarios assume that the catheter is inserted from a certain point in a specific direction at a uniform speed. But in real endovascular surgery, the angle and speed of insertion need to be controlled in real time. In the following

research, based on the existing model, the velocity and angle of the insertion point can be controlled to navigate the catheter. The controller in the simulation part can be completed using the *InterventionalRadiologyController* function in the plugin *Beamadapter*. In the experiment, the Cathbot platform can be used to control the movement of the catheter by operating the master device. And as mentioned before, the accuracy of this model-based approach largely depends on the accuracy of the model's physical parameters. In this paper, most of the parameters come from references, and have not been actually measured. If the accuracy physical parameters of the simulation model can be obtained through measurement, the accuracy of the model will be greatly improved.

As mentioned in section 3.4.2, the force obtained by simulation in an environment without simulated blood flow is much smaller than that in an environment with blood flow, and the simulated blood flow will make the insertion process of the catheter more realistic. But fluid mechanics remains limited in SOFA so far. Recently, I was pleasantly surprised to find that the developers of Sofa are improving the fluid plugin *SPHFluidForceField* based on Smoothed Particle Hydrodynamics (SPH) models. Maybe this plug-in can be used for blood flow simulation soon.

Bibliography

- [1] OECD and European Union. *Health at a Glance: Europe 2020*.
- [2] S. Christiansen, "What Is Endovascular Surgery?" 3 June 2021. [Online]. Available: <https://www.verywellhealth.com/endovascular-surgery-5100836>. [Accessed November 2022].
- [3] Kuhlemann, I., Kleemann, M., Jauer, P., Schweikard, A., & Ernst, F. (2017). Towards X-ray free endovascular interventions - using HoloLens for on-line holographic visualisation. *Healthcare technology letters*, 4(5), 184–187.
- [4] Duran, C., Estrada, S., O'Malley, M., Lumsden, A. B., & Bismuth, J. (2015). Kinematics effectively delineate accomplished users of endovascular robotics with a physical training model. *Journal of Vascular Surgery*, 61(2), 535-541.
- [5] Rafii-Tari, H., Riga, C. V., Payne, C. J., Hamady, M. S., Cheshire, N. J., Bicknell, C. D., & Yang, G. Z. (2016). Reducing contact forces in the arch and supra-aortic vessels using the Magellan robot. *Journal of vascular surgery*, 64(5), 1422–1432.
- [6] Amigo remote catheter system. Catheter Robotics, Inc. <https://www.catheterprecision.com/products/amigo/>. [Accessed January 2023].
- Duran, C., Estrada, S., O'Malley, M., Lumsden, A. B., & Bismuth, J. (2015). Kinematics effectively delineate accomplished users of endovascular robotics with a physical training model. *Journal of Vascular Surgery*, 61(2), 535-541.
- [7] Wang, F., Duratti, L., Samur, E., Spaelter, U., & Bleuler, H. (2007, August). A computer-based real-time simulation of interventional radiology. In *2007 29th Annual International Conference of the IEEE Engineering in Medicine and Biology Society* (pp. 1742-1745). IEEE.
- [8] Abdelaziz, M. E., Kundrat, D., Pupillo, M., Dagnino, G., Kwok, T. M., Chi, W., ... & Yang, G. Z. (2019, November). Toward a versatile robotic platform for fluoroscopy and mri-guided endovascular interventions: A pre-clinical study. In *2019 IEEE/RSJ International Conference on Intelligent Robots and Systems (IROS)* (pp. 5411-5418). IEEE.
- [9] Dagnino, G., Liu, J., Abdelaziz, M. E., Chi, W., Riga, C., & Yang, G. Z. (2018, October). Haptic feedback and dynamic active constraints for robot-assisted endovascular catheterization. In *2018 IEEE/RSJ International Conference on Intelligent Robots and Systems (IROS)* (pp. 1770-1775). IEEE.
- [10] Kundrat, D., Dagnino, G., Kwok, T. M., Abdelaziz, M. E., Chi, W., Nguyen, A., ... & Yang, G. Z. (2021). An MR-Safe endovascular robotic platform: Design, control, and ex-vivo evaluation. *IEEE transactions on biomedical engineering*, 68(10), 3110-3121.
- [11] Dagnino, G., Kundrat, D., Kwok, T. M., Abdelaziz, M. E., Chi, W., Nguyen, A., ... & Yang, G. Z. (2022). In-vivo Validation of a Novel Robotic Platform for Endovascular Intervention. *IEEE Transactions on Biomedical Engineering*.
- [12] Albarqouni, S., Konrad, U., Wang, L., Navab, N., & Demirci, S. (2016). Single-view X-ray depth recovery: toward a novel concept for image-guided interventions. *International journal of computer assisted radiology and surgery*, 11(6), 873-880.
- [13] Baur, C., Albarqouni, S., Demirci, S., Navab, N., & Fallavollita, P. (2016, August). Cathnets: detection and single-view depth prediction of catheter electrodes. In *International Conference on Medical Imaging and Augmented Reality* (pp. 38-49). Springer, Cham.
- [14] Delmas, C., Berger, M. O., Kerrien, E., Riddell, C., Troussset, Y., Anxionnat, R., & Bracard,

- S. (2015, March). Three-dimensional curvilinear device reconstruction from two fluoroscopic views. In *Medical Imaging 2015: Image-Guided Procedures, Robotic Interventions, and Modeling* (Vol. 9415, pp. 100-110). SPIE.
- [15] Razban, M., Dargahi, J., & Boulet, B. (2018, October). A sensor-less catheter contacts force estimation approach in endovascular intervention procedures. In *2018 IEEE/RSJ International Conference on Intelligent Robots and Systems (IROS)* (pp. 2100-2106). IEEE.
- [16] Back, J., Manwell, T., Karim, R., Rhode, K., Althoefer, K., & Liu, H. (2015, September). Catheter contact force estimation from shape detection using a real-time Cosserat rod model. In *2015 IEEE/RSJ International Conference on Intelligent Robots and Systems (IROS)* (pp. 2037-2042). IEEE.
- [17] Dawson, S. L., Cotin, S., Meglan, D., Shaffer, D. W., & Ferrell, M. A. (2000). Designing a computer - based simulator for interventional cardiology training. *Catheterization and cardiovascular interventions*, 51(4), 522-527.
- [18] TUAN, N. T., Myeongjin, K. I. M., & LEE, D. Y. A Hybrid Contact Model for Cannulation Simulation of ERCP.
- [19] Duriez, C., Cotin, S., Lenoir, J., & Neumann, P. (2006). New approaches to catheter navigation for interventional radiology simulation. *Computer aided surgery*, 11(6), 300-308.
- [20] Luboz, V., Blazewski, R., Gould, D., & Bello, F. (2009). Real-time guidewire simulation in complex vascular models. *The Visual Computer*, 25(9), 827-834.
- [21] Timoshenko, S. P. (1921). On the corrections for shear of the differential equation for transverse vibrations of prismatic bars, Lond. Edinburgh Dublin Philos. Mag. J. Sci, 41(245), 744-746.
- [22] Felippa, C. A., & Haugen, B. (2005). A unified formulation of small-strain corotational finite elements: I. Theory. *Computer Methods in Applied Mechanics and Engineering*, 194(21-24), 2285-2335.
- [23] Allard, J., Cotin, S., Faure, F., Bensoussan, P. J., Poyer, F., Duriez, C., ... & Grisoni, L. (2007, February). Sofa-an open-source framework for medical simulation. In *MMVR 15-Medicine Meets Virtual Reality* (Vol. 125, pp. 13-18). IOP Press.
- [24] SOFA-framework [Online]. Available: <https://www.sofa-framework.org/> [Accessed January 2023].
- [25] Faure, F., Duriez, C., Delingette, H., Allard, J., Gilles, B., Marchesseau, S., ... & Cotin, S. (2012). Sofa: A multi-model framework for interactive physical simulation. In *Soft tissue biomechanical modeling for computer assisted surgery* (pp. 283-321). Springer, Berlin, Heidelberg.
- [26] Product information of Impress® Hydrophilic Diagnostic Peripheral Catheters (<https://www.merit.com/peripheral-intervention/angiography/diagnostic-peripheral-catheters/impress-hydrophilic-catheters/#documents>) [Accessed November 2022]
- [27] Wei, Y., Cotin, S., Dequidt, J., Duriez, C., Allard, J., & Kerrien, E. (2012). A (near) real-time simulation method of aneurysm coil embolization. *Aneurysm*, 8(29), 223-248.]
- [28] Przemieniecki, J. S. (1985). Theory of matrix structural analysis. Courier Corporation.
- [29] Garland, M., & Heckbert, P. S. (1997, August). Surface simplification using quadric error metrics. In *Proceedings of the 24th annual conference on Computer graphics and interactive techniques* (pp. 209-216).
- [30] Garland, M., & Heckbert, P. S. (1998, October). Simplifying surfaces with color and texture

- using quadric error metrics. In Proceedings Visualization'98 (Cat. No. 98CB36276) (pp. 263-269). IEEE.
- [31] Sorkine, O. (2005). Laplacian mesh processing. *Eurographics (State of the Art Reports)*, 4, 4.
- [32] Duriez, C. (2013). *Real-time haptic simulation of medical procedures involving deformations and device-tissue interactions* (Doctoral dissertation, Université des Sciences et Technologie de Lille-Lille I).
- [33] Flores, P., Leine, R., & Glocker, C. (2011). Modeling and analysis of rigid multibody systems with translational clearance joints based on the non-smooth dynamics approach. In *Multibody dynamics* (pp. 107-130). Springer, Dordrecht.
- [34] Usui, M., Niki, H., & Kohno, T. (1994). Adaptive Gauss-Seidel method for linear systems. *International Journal of Computer Mathematics*, 51(1-2), 119-125.
- [35] Brandt-Wunderlich, C., Grabow, N., Schmitz, K. P., Siewert, S., & Schmidt, W. (2021). Cardiovascular catheter stiffness—a static measurement approach. *Current Directions in Biomedical Engineering*, 7(2), 721-723.
- [36] Goudot, G., Mirault, T., Bruneval, P., Soulat, G., Pernot, M., & Messas, E. (2019). Aortic wall elastic properties in case of bicuspid aortic valve. *Frontiers in Physiology*, 10, 299.
- [37] Coefficient of Friction Equation and Table Chart, Engineers Edge: [Online]. Available: https://www.engineersedge.com/coefficients_of_friction.htm [Accessed November 2022].
- [38] 张正友. *A flexible new technique for camera calibration*. Technical Report. 1998-10.
- [39] Jesús Lucio (2023). Bezier-curve [Online]. Available: <https://www.mathworks.com/matlabcentral/fileexchange/32817-bezier-curve>, MATLAB Central File Exchange. [Accessed January 2023].
- [40] Zachary Danziger (2023). Discrete Fréchet Distance [Online]. Available: <https://www.mathworks.com/matlabcentral/fileexchange/31922-discrete-frechet-distance>, MATLAB Central File Exchange. [Accessed January 2023]
- [41] Ma, H., Smal, I., Daemen, J., & van Walsum, T. (2020). Dynamic coronary roadmapping via catheter tip tracking in X-ray fluoroscopy with deep learning-based Bayesian filtering. *Medical image analysis*, 61, 101634.
- [42] Ambrosini, P., Ruijters, D., Niessen, W. J., Moelker, A., & van Walsum, T. (2015). Continuous roadmapping in liver TACE procedures using 2D–3D catheter-based registration. *International journal of computer assisted radiology and surgery*, 10(9), 1357-1370.